3-2022

Performance Assessment of Navigation Using Carrier Doppler Measurements from Multiple LEO Constellations

Michael J. Hartnett

PERFORMANCE ASSESSMENT OF NAVIGATION USING CARRIER DOPPLER MEASUREMENTS FROM MULTIPLE LEO CONSTELLATIONS

THESIS

Michael J. Hartnett

AFIT-ENG-MS-22-M-032

DEPARTMENT OF THE AIR FORCE
AIR UNIVERSITY

AIR FORCE INSTITUTE OF TECHNOLOGY

Wright-Patterson Air Force Base, Ohio

AFIT-ENG-MS-22-M-032

PERFORMANCE ASSESSMENT OF NAVIGATION USING CARRIER DOPPLER MEASUREMENTS FROM MULTIPLE LEO CONSTELLATIONS

THESIS

Presented to the Faculty

Department of Electrical and Computer Engineering

Graduate School of Engineering and Management

Air Force Institute of Technology

Air University

Air Education and Training Command

in Partial Fulfillment of the Requirements for the

Degree of Master of Science in Electrical Engineering

Michael J. Hartnett, B.S.

March 2022

AFIT-ENG-MS-22-M-032

PERFORMANCE ASSESSMENT OF NAVIGATION USING CARRIER DOPPLER MEASUREMENTS FROM MULTIPLE LEO CONSTELLATIONS

THESIS

Michael J. Hartnett, B.S.

Committee Membership:

Sanjeev Gunawardena, Ph.D.
Chair

David Woodburn, Ph.D.
Member

Gary Katulka, Ph.D.
Member

Abstract

The goal of this work is to characterize a novel navigation method which uses carrier Doppler shift measurements from Low Earth Orbit (LEO) satellites. An ever-growing reliance on the Global Navigation Satellite System (GNSS) has coincided with an increase in ways it can be degraded or denied, whether naturally occurring or man-made. These potentially disastrous threats to traditional navigation and timing have necessitated new technologies to augment GNSS in the case of an outage. LEO constellations, whose size and higher signal power make them potentially useful for navigation, are one technology that has been explored. The navigation algorithms detailed in this research use Doppler measurements from 8 or more LEO satellites to simultaneously solve for position, clock offset, velocity, and clock offset rate. Through simulation, a user-satellite geometry analysis is conducted for a number of emerging LEO constellations, as well as navigation simulations with the same constellations. Results are presented which show promise from both a satellite geometry perspective and position, velocity, and time (PVT) solution convergence perspective.

Acknowledgements

I would like to thank my advisor, Dr. Gunawardena, and my mentor, Dr. Katulka, for their technical expertise and invaluable advice during my research and writing of this document. I would also like to thank Dr. Psiaki for the guidance provided when questions arose. Finally, I'd like to thank my family and friends for their support and understanding during this endeavor.

Michael J. Hartnett

Table of Contents

Page

List of Figures

List of Tables

List of Acronyms

AFB	Air Force Base
BPSK	Binary Phase-Shift Keying
CoC	Constellation of Constellations
dB	Decibels
DOP	Dilution of Precision
ECEF	Earth-Centered Earth-Fixed
FCC	Federal Communications Commission
GDOP	Geometric Dilution of Precision
GHz	Gigahertz
GNSS	Global Navigation Satellite System
GPS	Global Positioning System
HDOP	Horizontal Dilution of Precision
Hz	Hertz
IMU	Inertial Measurement Unit
INS	Inertial Navigation System
LEO	Low Earth Orbit
MCS	Master Control Station

MEO	Medium Earth Orbit
MHz	Megahertz
NORAD	North American Aerospace Defense Command
PRN	Pseudo-Random Noise
PVT	Position, Velocity, and Time
RMS	Root Mean Square
SDR	Software Defined Radio
STAN	Simultaneous Tracking and Navigation
SV	Space Vehicle
TLE	Two-Line Element
UHF	Ultra High Frequency
VDOP	Vertical Dilution of Precision
VHF	Very High Frequency

PERFORMANCE ASSESSMENT OF NAVIGATION USING CARRIER DOPPLER MEASUREMENTS FROM MULTIPLE LEO CONSTELLATIONS

1. Introduction

1.1 Background

Navigation can be defined as the simultaneous calculation of a body's three-dimensional position and time relative to a given coordinate system. A number of different tools can be used to navigate: a compass and map, a Global Navigation Satellite System (GNSS) receiver, an inertial navigation system (INS), or multiple navigation sensors can be combined with a Kalman filter. As the world has become more and more reliant on GNSS, of which the Global Positioning System (GPS) is a member, it has opened up a severe vulnerability. Much of the US infrastructure relies on GPS and would not be able to function, without a backup, in the event of a GPS outage. A study found that a GPS outage could cost $1 billion per day to the US economy [41]. There has been a major push in the defense and commercial markets to develop technologies that help to augment GNSS. Whether natural obstructions to GNSS or intentional interference, navigation methods independent of GNSS are more necessary than ever before.

1.2 Motivation

Traditional GNSS navigation uses satellites that orbit the Earth in what is considered Medium Earth Orbit (MEO) at around 20,000 kilometers above sea level [3]. Historically, there have been several instances of navigation systems operating in Low

Earth Orbit (LEO), but nothing as robust as GNSS. In the past 5-10 years, there has been a major surge in commercial entities launching, or planning to launch, large LEO constellations to provide different communication services. An increasingly popular research area has been exploring the possibility of leveraging these larger LEO constellations for navigation. The motivation behind this thesis is to expand upon one such paper that introduced a LEO-based navigation method [38]. The navigation method uses carrier Doppler shift measurements from 8 LEO satellites to simultaneously solve for position, receiver clock offset, velocity, and receiver clock offset rate. The original research utilized a single LEO constellation, whereas this research investigates the use of multiple different constellations for navigation. A primary goal of this research is to evaluate the suitability of these LEO constellations in the navigation method proposed.

1.3 Approach

The approach taken to facilitate this research was through the use of a navigation simulation using the Python programming language. The navigation equations derived throughout this document were used to implement a simulated receiver navigation engine. The required ephemeris parameters for the orbit propagator in the simulation used two sources. Publicly available LEO satellite orbital parameters were used for the already launched vehicles. For the yet-to-be-launched vehicles, the orbital parameters were fabricated using published information about the constellation. Simulation scenarios and receiver initial conditions were in part derived from previous research [38], though additional scenarios are also considered in an attempt to further the work. The test scenarios were simulated a total of 100 times with each different LEO constellation to aid in the formation of observations and conclusions. Simulated receiver convergence rate, number of filter iterations, and the final receiver state er-

rors are the metrics used to determine the success or failure of a given simulation. Additional techniques are derived to present the ability of a constellation to provide the coverage and geometry necessary for navigation. The results and analysis from these techniques are also presented.

1.4 Related Work

The work that this research is heavily based on is presented in [38]. Psiaki proposed a novel navigation method that uses carrier Doppler shift measurements from 8 LEO satellites to solve for position, clock offset, velocity, and clock offset rate. A simulation is developed with an earlier version of the proposed Starlink constellation which resulted in sub-10 meter position accuracies [8]. Geometric Dilution of Precision (GDOP) analysis is also presented for different versions of the proposed Starlink and OneWeb constellations [5].

The navigation method introduced in [38] is researched further in [32]. McLemore and Psiaki employ the use of a Kalman filter to combine the solutions from the LEO Doppler measurements and an inertial measurement unit (IMU). A comparison of the effect of satellite signal availability and the grade of IMU was performed using a simulated flight path. Sub-meter level performance was presented for the best case scenario, with position errors on the order of 5 meters presented for the worst case IMU and signal availability.

In [39], Reid et al. researched the possibility of leveraging large LEO constellations to augment GNSS, or even act as a standalone backup to it. The work performed a thorough dilution of precision (DOP) analysis for several planned LEO constellations and compared against other GNSS constellations. With the improved DOP values, a trade study was conducted to assess what accuracy would be necessary, from LEO ephemeris and timing messages, in order to match the performance of GNSS. A hosted

payload design that utilizes lower cost alternative technologies than those of GNSS is proposed.

Prata et al. researched the possibility of outfitting LEO satellites with a multi-band GNSS receiver for precise tracking and orbit determination in [13]. The main goal of this research is to provide highly accurate position, velocity, and time (PVT) (10 cm, 0.1 mm/sec, 5 ns) to objects in LEO. To date, only ground-based tests have been conducted, but the results from the multi-band GNSS receiver are promising.

In [12], Ardito et al. also research the aiding of an INS with both pseudorange and Doppler observables from LEO satellites. The work simulates an INS with access to GPS for a predetermined amount of time, during which the navigation system is tracking and improving its estimate of LEO satellite states. Once GPS is denied, the system uses a simultaneous tracking and navigation (STAN) framework to simultaneously track the LEO satellite states and navigate. Two sets of cases were tested. The first set of cases only employ the INS following denial of GPS while the second set utilizes the INS tightly-coupled with LEO measurements. Following a 10 minute simulation, Root mean square (RMS) and final errors are improved by several orders of magnitude when LEO measurements are included in the solution.

In [28], [31], [34], and [35], Kassas et al. explore different techniques to simultaneously track LEO satellites and characterize their state vectors. The work in [28] uses a receiver with a known position to track LEO signals and extract their pseudorange and Doppler observables. A method is developed to use these observables to provide satellite ephemeride estimates that are improved from only using an orbit propagator. The improved satellite ephemerides are then used to localize a receiver with an unknown position and compared against the performance with propagated ephemerides. The results show improvements in both the satellite ephemeris accuracy and receiver positioning accuracy. The research in [31] focuses on machine learning

frameworks to aid in STAN with LEO satellites. Several machine learning techniques are explored with the most fruitful technique achieving a 3-D RMS error of 3.6 meters following a 30 second ground-vehicle trajectory of 871 meters. This is compared to a LEO-aided INS which achieved a 3-D RMS error of 30 meters. The work in [34] and [35] also focuses on a STAN technique that shows results better than those of a simple orbit propagator. The improved satellite ephemerides are used in a LEO-aided INS scenario, which result in better 3-D accuracy than a GPS-denied INS-only solution.

In [25], Gutt et al. demonstrate the timing accuracy that can be achieved when using a LEO receiver to discipline different types of clocks. Apart from the excellent timing produced from the LEO-disciplined clocks, the work highlights one major advantage LEO signals have over GNSS. One of the test scenarios involves a LEO receiver tracking signals from the Iridium constellation in an indoor office environment. The higher received signal power provided from LEO allows the receiver to track in areas GNSS could not reach.

Research in [16], [27], [30], and [37] utilized software defined radios (SDRs) to blindly track signals from in-orbit LEO satellites. In [16], the authors developed a multi-constellation SDR and demonstrated its ability to derive receiver position, receiver clock drift, and satellite clock drift from Doppler shift measurements from LEO downlink signals. This work used signals from both Iridium and Orbcomm satellites to generate a position accuracy of 172 meters. Both [27] and [37] used a SDR design similar to Figure 1.1 to blindly track signals from the Starlink constellation. The stationary receiver was able to successfully measure the Doppler shift from 6 Starlink satellites and achieve a sub-35 meter 3-D position accuracy. In [27], Kassas et al. also provides a satellite coverage and DOP analysis of the proposed Starlink constellation. Work in [30] employed a Kalman filter and Doppler shift measurements from 2 Orbcomm LEO satellites to achieve a position accuracy of 360 meters after 1

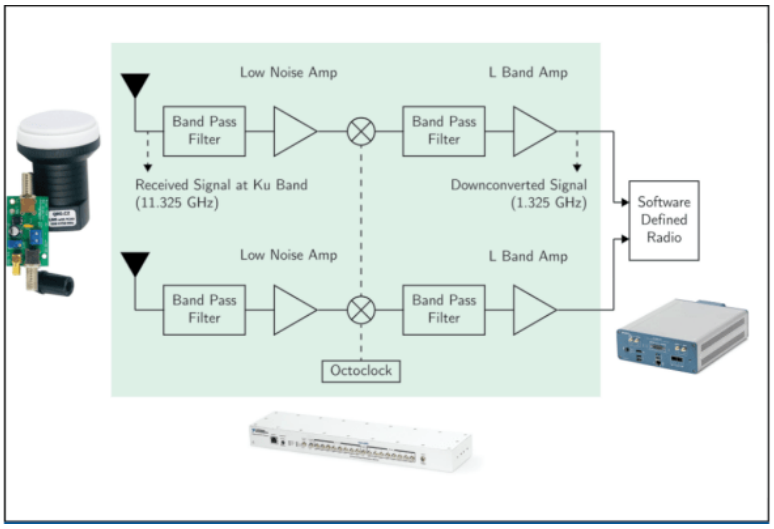

Figure 1.1. Example LEO software defined receiver design [27]

minute.

In [29] and [42], the research focuses on navigation using real LEO signals in a base and rover configuration. The approach taken in [29] is where the base station is at a known stationary position and it communicates this position, along with LEO carrier phase observables, to the rover. The rover uses the known position from the base station and its own carrier phase observables to derive its position. Using signals from Orbcomm satellites, this method resulted in a sub-15 meter position error. The research in [42] uses a similar base station and rover approach but does not require knowledge of satellite states. The base station performs an angle-of-arrival measurement on a blindly tracked LEO signal and derives its azimuth and elevation. The base provides these azimuth and elevation estimates to the rover. With azimuth and elevation and differential Doppler positioning, the rover can solve for its position without knowledge of the satellite states. The benefit of this method is that it is constellation agnostic and overcomes the problem of lack of knowledge of transmitter states.

1.5 Outline

The remainder of this work will be presented in the following format. Chapter 2 will provide the necessary mathematical background for derivation of the navigation equations, as well as some general navigation background. Chapter 3 introduces the different LEO constellations considered, the navigation equation derivations, and a description of the simulation. Chapter 4 presents the results from the research along with observations and analysis. Finally, Chapter 5 provides an overall summary of the research, including the contributions made and limitations of the research. Recommendations for future work based on this research are additionally included.

2. Background

2.1 Mathematical Notation

The following mathematical notation will be used throughout this document:

Scalars: Scalar quantities are denoted by uppercase or lowercase italicized characters, such as a or A.

Vectors: Vectors are denoted by lower case italicized characters with an arrow on top, such as $\vec{a}$ or $\vec{b}$. All vectors are assumed to be column vectors unless otherwise stated.

Matrices: Matrices are denoted as lowercase or uppercase boldface characters, such as $\boldsymbol{\omega}$ or $\boldsymbol{A}$.

Derivatives: Derivatives are denoted using dots above a character or symbol. The first derivative of $\vec{v}$ is denoted as $\dot{\vec{v}}$. All subsequent derivatives are denoted with additional dots.

Partial Derivatives: Partial derivatives are denoted as $\frac{\partial}{\partial}$, where $\frac{\partial}{\partial x}\boldsymbol{A}$ is the partial derivative of $\boldsymbol{A}$ with respect to x. Within equations, partial derivatives are also denoted by $\partial_x \boldsymbol{A}$ as shorthand. The two partial derivative notations here should be considered equivalent throughout the thesis.

Transpose: The transpose of a vector or matrix is denoted with a superscript of $\top$. $\vec{a}^\top$ denotes the transpose of the vector $\vec{a}$.

Unit Vectors: A unit vector is a vector of length 1. The unit vector of $\vec{\rho}$ is equal to each component of $\vec{\rho}$ divided by the magnitude of the vector, $\frac{\vec{\rho}}{||\vec{\rho}||}$. Unit vectors are denoted with a hat, $\hat{\rho}$.

Superscripts: Unless otherwise stated, superscripts will denote the satellite index of a scalar, vector, or matrix. For example, a^n, $\vec{b}^n$, and $\boldsymbol{A}^n$ are values associated with the n^{th} satellite.

Subscripts: Unless otherwise stated, subscripts will be used as descriptors to differentiate between identically denoted variables. For example, δt^n_{trop} and δt^n_{ion} denote the time delay from the n^{th} satellite caused by the troposphere and ionosphere, respectively.

Vector Components: A secondary use of subscripts is to denote components of a vector or matrix. Individual vector components that represent a scalar value are denoted by a subscript corresponding to a particular axis, as in $\vec{r}_x$. Matrix components that represent a row vector are similarly denoted by a subscript corresponding to a particular axis, as in $\boldsymbol{A}_y$.

Function Notation: Functions and their inputs are denoted using parentheses. Matrix $\boldsymbol{A}$ as a function of x is denoted as $\boldsymbol{A}(x)$. Similarly, vector $\vec{r}$ as a function of t is denoted as $\vec{r}(t)$.

Gradient: The gradient of a function, ∇, is a vector consisting of the partial derivatives of the function.

$$\nabla f(x,y) = \left[\frac{\partial f}{\partial x}, \frac{\partial f}{\partial y}\right]$$

Hessian: The Hessian matrix of a function, ∇^2, is a square matrix consisting of the second-order partial derivatives of the function.

$$\nabla^2 f(x,y) = \begin{bmatrix} \frac{\partial^2 f}{\partial x^2} & \frac{\partial^2 f}{\partial x \partial y} \\ \frac{\partial^2 f}{\partial y \partial x} & \frac{\partial^2 f}{\partial y^2} \end{bmatrix}$$

Root Mean Square: The root mean square is the square root of the mean square, where the mean square is the average of the squares of a set of numbers [7].

2.2 Gauss-Newton Method

The Gauss-Newton method is often used as a method to solve nonlinear least-squares problems. Nonlinear least-squares optimization involves using m observations to solve for n unknowns using a model that is nonlinear, where $m \geq n$. The Gauss-Newton method works by minimizing the cost function, $J(x)$,

$$J(x) = \sum_{i}^{m} r_i^2 \tag{2.1}$$

$$r_i = h_i(x) - y, \tag{2.2}$$

where $h_i(x)$ is the nonlinear measurement model function that predicts a measurement, y is a measurement, and r_i are the residuals. The minimization of this cost function yields the least-squares estimate. The Gauss-Newton method is a modification of the Newton method.

Differentiating Equation 2.1 with respect to x_j yields

$$\frac{\partial}{\partial x_j} J(x) = \sum_{i}^{m} \frac{\partial r_i}{\partial x_j} r_i. \tag{2.3}$$

The gradient of J is

$$\nabla J = \mathbf{H}^\top \vec{r}, \tag{2.4}$$

where $\mathbf{H}$ is an m-by-n Jacobian matrix. Differentiating again, this time with respect to x_k, yields

$$\frac{\partial^2}{\partial x_j \partial x_k} J(x) = \sum_{i}^{m} \left(\frac{\partial r_i}{\partial x_j} \frac{\partial r_i}{\partial x_k} + \frac{\partial^2 r_i}{\partial x_j \partial x_k} r_i \right), \tag{2.5}$$

where the Hessian of J is

$$\nabla^2 J = \mathbf{H}^\top \mathbf{H} + \mathbf{Q}. \tag{2.6}$$

$\mathbf{Q}$ represents the second order partial derivatives that can become impractical to

compute, which the Gauss-Newton method ignores. This is where the Gauss-Newton method differs from the Newton method.

The method is initialized with an initial guess, $\vec{x}_i$, and an update to that guess is calculated using the Jacobian matrix.

$$\Delta\vec{x} = (\mathbf{H}^\top \mathbf{H})^{-1}\mathbf{H}\vec{r} \tag{2.7}$$

$$\vec{x}_{i+1} = \vec{x}_i + \Delta\vec{x} \tag{2.8}$$

In order to avoid divergence and ensure the $\Delta\vec{x}$ update is not too large, a slight modification to the Gauss-Newton method can be made. Often called a damped Gauss-Newton method, a comparison of the old and new cost functions can be made prior to applying the update. The sequence of this method as it would be implemented in code is shown below. The cost function (J), residuals ($\vec{r}$), and Jacobian matrix

```
Initial guess x_i
while Δx > some value do
    Compute J and r
    Compute Δx
    x_temp = x_i + Δx
    Compute J_new using x_temp
    while J_new > J do
        Δx = Δx/2
        x_temp = x_i + Δx
        Compute J_new using x_temp
    end while
    x_{i+1} = x_i + Δx
end while
```

($\mathbf{H}$) are calculated using the initial guess ($\vec{x}_i$). The update ($\Delta\vec{x}$) is then calculated and applied to find a new cost function (J_{new}). The damping occurs if the new cost is larger than the old cost function – the update is halved if this is the case, and the process is repeated until the new cost is less than the old. This sequence continues

until an exit condition is met, which in the scenario above is when $\Delta\vec{x}$ falls below a certain value. The damping value and the exit condition are not universally standard and will depend on the problem [23] [24].

2.3 Global Positioning System

GPS is a satellite based radio navigation system operated by the United States Space Force. The first GPS satellite was launched on February 22nd, 1978 and the constellation became fully operational in 1993. Typical GPS receivers require signals from 4 different satellites in order to derive accurate position and time. Position and time are derived using a technique called trilateration, which involves measuring distances. Figure 2.1 depicts an example of trilateration using 4 satellites. Three dimensional position and time represent 4 unknowns that a receiver is trying to solve for – the distance from 4 satellites satisfies the 4 unknowns. A minimum of 24 satellites are necessary for GPS to provide adequate coverage over the entire globe and be considered fully operational. Anywhere between 24 and 32 satellites are operational at one time with 30 currently in orbit, arranged such that 6 satellites are in view at any given time from anywhere on the Earth. GPS consists of three segments – the Space Segment, the Control Segment, and the User Segment [33].

2.3.1 Space Segment

Unsurprisingly, the 30 operational satellites represent the Space Segment portion of GPS. The satellites fly in MEO at approximately 20,000 kilometers (12,500 miles) from the Earth's surface. The orbital period of GPS satellites is 12 hours, meaning they circle the Earth twice per day and depending on the location on Earth, each satellite is visible for up to several hours at one time. The GPS constellation consists of 6 orbital planes, with 4-6 satellites per plane, flying at an inclination of approximately

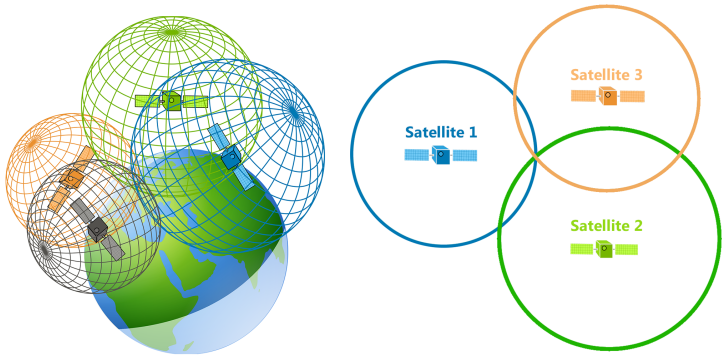

Figure 2.1. Trilateration [2]

55 degrees. A rendering of the GPS constellation is shown in Figure 2.2.

GPS satellites continually transmit a modulated carrier wave signal which GPS receivers use to calculate position and time. GPS utilizes the L-band to transmit its signal – L1 (1575.42 MHz), L2 (1227.60 MHz), and L5 (1176.45 MHz). The signal contains information, specifically transmission time and satellite position data, that the receiver can use in conjunction with its own time reference to derive a PVT solution. In order for the satellites to transmit accurate data, they themselves must keep accurate records of their time and position. Each GPS satellite carries multiple atomic clocks to contribute to accurate signal timing on the order of nanoseconds. An ephemeris message, which includes orbital information for the transmitting satellite, is transmitted to help provide accurate satellite position. With the transmission time and time of arrival of the signal, a receiver can calculate the pseudorange between itself and a satellite because of the nature of radio waves. Radio waves travel at the speed of light, a known constant, making it trivial to calculate pseudorange given the signal propagation time. The term pseudorange is used to denote an approximate range due to the inevitable errors in the measured signal propagation time. Trilateration can

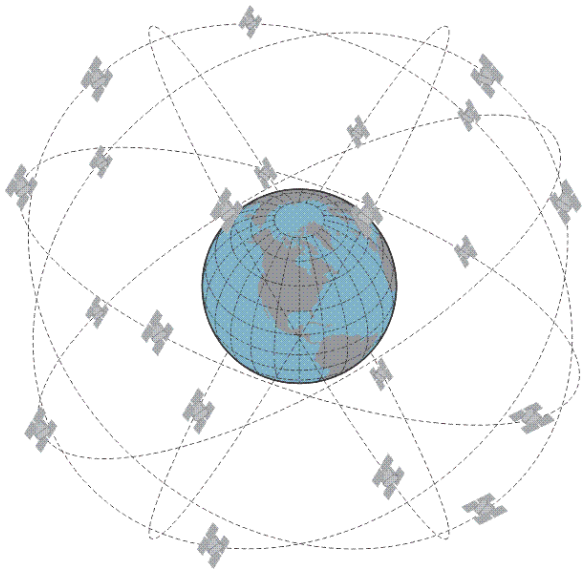

Figure 2.2. GPS constellation (not to scale) [4]

be performed once signals from 4 satellites have been received.

2.3.2 Control Segment

The entity in charge of ensuring satellites are operating correctly is known as the GPS Control Segment (also referred to as Ground Segment). The Control Segment consists of a Master Control Station (MCS), located at Schriever Air Force Base (AFB), CO, dedicated GPS ground antennas, and dedicated monitor stations. Figure 2.3 depicts a map of the Control Segment infrastructure. The primary responsibility of the MCS is to monitor each satellite and provide navigational updates when necessary. Updates involve synchronizing the atomic clocks on board the satellites and providing orbital model updates critical to ensuring accurate ephemeris messages. Monitoring satellites and sending updates is facilitated by the monitoring stations and ground antennas around the globe. The Control Segment plays an integral role in the reliability and precision of navigation using GPS.

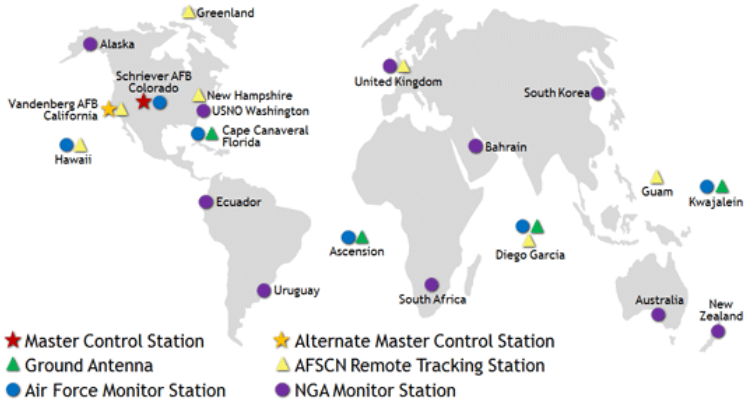

Figure 2.3. The Control Segment [1]

2.3.3 User Segment

As mentioned in the previous sections, GPS receivers generate PVT by using the modulated carrier signal transmitted by satellites. To allow receivers to identify which satellites they are receiving signals from, the carrier signal is modulated with a pseudo-random noise (PRN) code unique to each satellite. A PRN code is a binary sequence that appears to be random but is actually deterministic and can be generated at any given state. Each GPS satellite transmits its own PRN code. The navigation message, containing transmission time and satellite ephemeris, is also modulated with the carrier signal. GPS uses binary phase-shift keying (BPSK) modulation to combine the signal and the data. For receivers to demodulate the signal and make use of the navigation data, they keep a bank of PRN codes that correlate with the PRN codes being transmitted. Autocorrelation functions are used between each of the receiver PRN codes and the incoming signal to determine which satellite it came from. PRN codes are designed such that they have little cross-correlation when non-matching codes are correlated or the code phase is not aligned, but a clear peak is present when matching codes are correlated and their phases match. Once the signal has

been demodulated, the receiver can make use of the data and generate several GPS observables.

2.3.3.1 Pseudorange

The observable that a majority of GPS receivers rely on to generate PVT solutions are pseudorange measurements. A pseudorange is the "pseudo" distance between a satellite and receiver. Navigation messages and PRN codes transmitted from satellites are designed so that a receiver, with its own set of PRN codes, can easily determine the transmit and receive time of the signals. This is known as the signal propagation time and can be multiplied by the speed of light to give the pseudorange. Figure 2.4 shows that there are also errors present in the propagation time calculation that need to be taken into effect. The clocks on each satellite and GPS receiver introduce error into the calculation. However, satellite clock errors are minimized with the help of the control segment, which make receiver clocks the dominant error source. As has been mentioned, simultaneous pseudorange measurements from 4 satellites can be used to derive three dimensional position and time. The traditional pseduorange

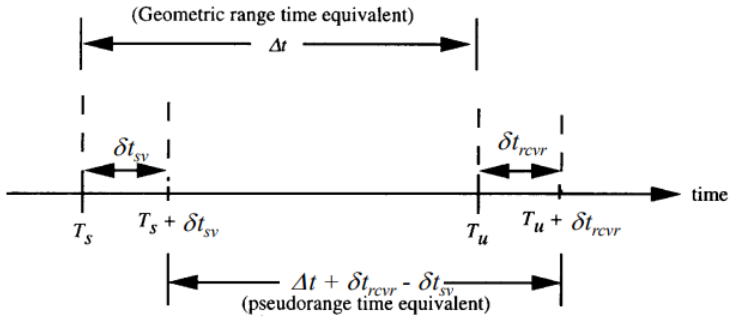

Figure 2.4. GPS signal propagation time calculation [26]

measurement equation can be found in Equation 2.9,

$$\rho^j = \sqrt{(r_x^j - r_x)^2 + (r_y^j - r_y)^2 + (r_z^j - r_z)^2} + c\delta t_r \tag{2.9}$$

where r_x^j, r_y^j, and r_z^j is the Earth-Centered Earth-Fixed (ECEF) position of a satellite, c is the speed of light, r_x, r_y, and r_z, is the unknown ECEF position of a receiver, and δt_r is the unknown receiver clock error. With 4 psuedorange measurements, the 4 unknowns can be solved for.

2.3.3.2 Doppler Shift

The Doppler effect, or Doppler shift, is the change in frequency of a transmitted signal due to the relative motion between the transmission source and observer. A simple example of Doppler shift that almost everyone has been exposed to, but not necessarily noticed, is emergency vehicle sirens. A stationary observer will hear a higher pitched siren when a firetruck is moving towards them, as compared to when it is moving away. The same concept applies to the GPS signal received by users on the Earth's surface. The Doppler equation is

$$f_o = \frac{c \pm v_o}{c \pm v_s} f_s, \tag{2.10}$$

where f_s and v_s are the transmitted frequency and velocity at the source of the signal, and f_o and v_o are the received frequency and velocity of the observer. Velocity of the source and observer is added or subtracted depending on the direction. As a GPS receiver observable, Doppler shift will be negative if the satellite is moving away from the receiver and positive when moving towards the receiver. While pseudorange is the dominant observable used for navigation, Doppler shift can also be used, which will be explored in Section 2.6.

2.3.3.3 Carrier-Phase

In simple terms, the carrier-phase measurement between a receiver and a satellite is a measure of the range given in cycles of the carrier frequency. Because the carrier wavelength is known, the carrier-phase measurement is very precise (on the order of millimeters). However, the actual number of cycles between the receiver and satellite is not measurable, which is known as the carrier-phase ambiguity. Figure 2.5 is an example of a carrier-phase measurement, where "measured" is the calculated value and "ambiguity" is the portion of the value that cannot be resolved. A good analogy for this is to imagine a rope, with knots every 20 centimeters, stretching from a receiver to a satellite. It's easy to precisely measure the distance between the receiver and the closest knot, but it's impossible to know how many knots exist between the receiver and satellite. There are methods, which will not be discussed in this thesis, for resolving the carrier-phase ambiguity [33].

2.4 Keplerian Orbital Elements

Orbital elements are the parameters that can be used to describe the orbit of a given satellite or body in space. There are 6 orbital elements traditionally used in orbit determination, called Keplerian elements after Johannes Kepler. The definitions from [6] are provided below.

Eccentricity (e): is the shape of an ellipse, describing how much it is elongated compared to a circle.

Semimajor Axis (a): is the sum of the periapsis and apoapsis distances divided by two. For two-body orbits, the semimajor axis is the distance between the centers of the bodies.

Eccentricity and semimajor axis are used to define the shape and size of the orbital ellipse.

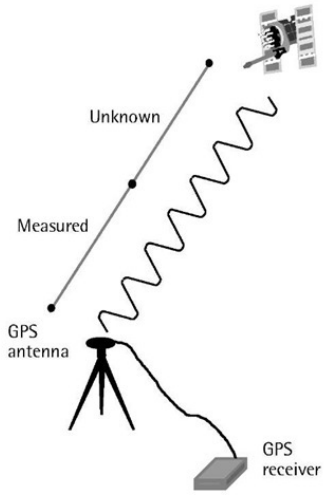

Figure 2.5. Carrier-Phase measurement [33]

Inclination (i): is the vertical tilt of the ellipse with respect to the reference plane, measured at the ascending node.

Longitude of the Ascending Node (Ω): horizontally orients the ascending node of the ellipse with respect to the reference frame's vernal point (γ).

Inclination and longitude of the ascending node are used to define the orientation of the orbital plane where the ellipse resides.

Argument of Periapsis (ω): defines the orientation of the ellipse in the orbital plane, as an angle measured from the ascending node to the periapsis.

True Anomaly at Epoch (ν): defines the position of the orbiting body along the ellipse at a specific time (the epoch).

Figure 2.6 provides a diagram which includes the 6 traditional orbital elements. For satellites that orbit the Earth, the reference plane would be in the Earth's equatorial plane.

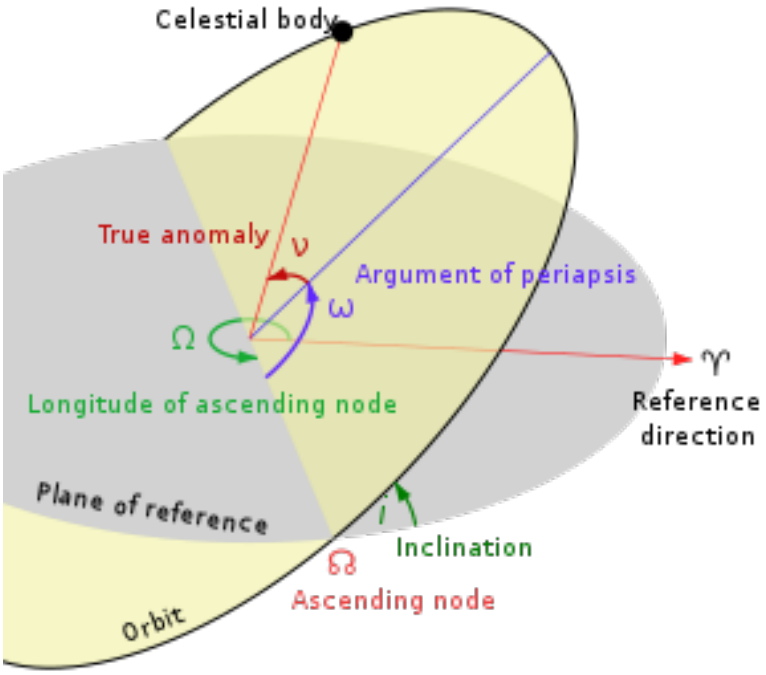

Figure 2.6. Keplerian Orbital Elements [6]

2.5 Receiver Initialization State

The ability of, and speed at which, a GPS receiver (or other satellite based navigation device) can converge on a correct solution is dependent on a number of factors. A large factor is the state in which a receiver is powered on and initialized. The three main receiver initialization states are cold start, warm start, and hot start. A cold start is the most difficult scenario, where the receiver has no prior knowledge of its position, velocity, time, or satellite locations. Often times, a cold-started receiver will report PVT values of 0 until it is able to track satellites and generate a usable solution. In a warm start scenario, the receiver typically has an estimate of the current time within 20 seconds, current position within 100 kilometers, and velocity within 25 m/sec. The receiver would also have some prior knowledge of satellite locations. A hot start scenario provides the receiver with accurate position, time, and satellite

ephemeris data upon startup. This enables rapid signal acquisition [9].

2.6 Geometric Dilution of Precision

GDOP is a metric used in satellite navigation to describe the mathematical effect of satellite geometry on receiver position and time errors. GDOP values range from < 1 to well over 100, with < 2 being excellent, $2 - 10$ being moderate, and anything over 20 being poor. The GDOP calculation for pseudorange based navigation systems is shown in the following equations.

$$\mathbf{A} = \begin{bmatrix} \frac{r_x^1 - r_x}{||\vec{r}^1||} & \frac{r_y^1 - r_y}{||\vec{r}^1||} & \frac{r_z^1 - r_z}{||\vec{r}^1||} & -1 \\ \frac{r_x^2 - r_x}{||\vec{r}^2||} & \frac{r_y^2 - r_y}{||\vec{r}^2||} & \frac{r_z^2 - r_z}{||\vec{r}^2||} & -1 \\ \vdots & \vdots & \vdots & \vdots \\ \frac{r_x^j - r_x}{||\vec{r}^j||} & \frac{r_y^j - r_y}{||\vec{r}^j||} & \frac{r_z^j - r_z}{||\vec{r}^j||} & -1 \end{bmatrix} \tag{2.11}$$

Once again, r_x^j, r_y^j, and r_z^j is the ECEF position of a satellite and r_x, r_y, and r_z, is the ECEF position of a receiver. The first 3 columns of $\mathbf{A}$ represent the components of the unit vector from the receiver to each respective satellite.

$$\mathbf{Q} = (\mathbf{A}^\top \mathbf{A})^{-1} = \begin{bmatrix} \sigma_{xx} & \sigma_{xy} & \sigma_{xz} & \sigma_{xt} \\ \sigma_{xy} & \sigma_{yy} & \sigma_{yz} & \sigma_{yt} \\ \sigma_{xz} & \sigma_{yz} & \sigma_{zz} & \sigma_{zt} \\ \sigma_{xt} & \sigma_{yt} & \sigma_{zt} & \sigma_{tt} \end{bmatrix} \tag{2.12}$$

$\mathbf{Q}$ is the covariance matrix, and several DOP metrics can be derived from its values, where PDOP is the position dilution of precision and TDOP is the time dilution of precision.

$$PDOP = \sqrt{\sigma_{xx} + \sigma_{yy} + \sigma_{zz}}$$

$$TDOP = \sqrt{\sigma_{tt}}$$

$$GDOP = \sqrt{PDOP^2 + TDOP^2}$$

The horizontal dilution of precision (HDOP) and vertical dilution of precision (VDOP) can be also be calculated following a coordinate conversion. An alternative GDOP calculation for the navigation method described in this thesis will be presented in Section 3.4.

2.7 Two-Line Element Sets

A Two-Line Element (TLE) set is a data format containing orbital characteristics for a given object orbiting the Earth at a given time, or epoch. The North American Aerospace Defense Command (NORAD) tracks and generates TLE data for every body of significant size, including space debris as small as 10 centimeters in diameter [36]. Along with a propagation model, the position and velocity of a space vehicle can be predicted at any time using TLE data. The position error at epoch is on the order of kilometers, however, and continues to grow as time diverges from epoch. Because of the limited accuracy inherent with using TLE files, their use is better suited for a simulated environment as opposed to real-world receivers. This thesis explores the use of currently in-orbit LEO satellites as well as those not yet launched for the purpose of navigation. To achieve this, a combination of NORAD-maintained and fabricated TLE files are used. An example TLE file can be found in Figure 2.7 and a description of the data fields can be found in Figure 2.8.

```
ISS (ZARYA)
1 25544U 98067A   08264.51782528 -.00002182  00000-0 -11606-4 0  2927
2 25544  51.6416 247.4627 0006703 130.5360 325.0288 15.72125391563537
```

Figure 2.7. Example TLE Set [11]

Field	Columns	Content	Example
1	01–24	Satellite name	ISS (ZARYA)

Field	Columns	Content	Example
1	01	Line number	2
2	03–07	Satellite Catalog number	25544
3	09–16	Inclination (degrees)	51.6416
4	18–25	Right ascension of the ascending node (degrees)	247.4627
5	27–33	Eccentricity (decimal point assumed)	0006703
6	35–42	Argument of perigee (degrees)	130.5360
7	44–51	Mean anomaly (degrees)	325.0288
8	53–63	Mean motion (revolutions per day)	15.72125391
9	64–68	Revolution number at epoch (revolutions)	56353
10	69	Checksum (modulo 10)	7

Field	Columns	Content	Example
1	01	Line number	1
2	03–07	Satellite catalog number	25544
3	08	Classification (U: unclassified, C: classified, S: secret) [11]	U
4	10–11	International Designator (last two digits of launch year)	98
5	12–14	International Designator (launch number of the year)	067
6	15–17	International Designator (piece of the launch)	A
7	19–20	Epoch year (last two digits of year)	08
8	21–32	Epoch (day of the year and fractional portion of the day)	264.51782528
9	34–43	First derivative of mean motion; the ballistic coefficient [12]	-.00002182
10	45–52	Second derivative of mean motion (decimal point assumed) [12]	00000-0
11	54–61	B^*, the drag term, or radiation pressure coefficient (decimal point assumed) [12]	-11606-4
12	63–63	Ephemeris type (always zero; only used in undistributed TLE data) [13]	0
13	65–68	Element set number. Incremented when a new TLE is generated for this object. [12]	292
14	69–69	Checksum (modulo 10)	7

Figure 2.8. Definition of TLE parameters: Top Left: title line, Bottom Left: line 2, Right: line 1 [11]

2.8 LEO vs. MEO

The majority of Chapter 2 has been dedicated to providing background on navigation using GPS satellites, which operate in MEO. MEO orbits have an altitude between 2,000 kilometers and approximately 36,000 kilometers. LEO satellites operate at an altitude below 2,000 kilometers. GPS satellites orbit the Earth twice per day while LEO constellations have an orbital period of less than 128 minutes, meaning they orbit the Earth at least 11.25 times per day. This difference in orbital periods also means that while GPS satellites are visible for hours at a time, LEO satellites are visible for less than 15 minutes at a time.

2.8.1 Comparison of LEO Satellites to GPS

Altitude is not the only differentiator between the GPS constellation and LEO constellations. As a function of the satellites operating at significantly different altitudes, there are several other differences between MEO and LEO constellations.

One major advantage that LEO satellites' proximity to the Earth results in is

signal strength. A LEO signal received on the surface of the Earth can be up to 1,000 times (30 decibels (dB)) stronger than GPS. The stronger signal means that LEO signals potentially have better penetration through obstructions, lessen the effects of multipath, and have better resistance to interference. LEO signals theoretically can reach areas that traditional GPS cannot, potentially even indoors. Conversely they can transmit 30 dB less power and generate the same received signal strength.

Because GPS satellites orbit at such a high altitude, they can provide a much larger signal footprint. Each GPS satellite provides a signal footprint approximately 12,000 kilometers in diameter, while LEO satellites can provide roughly 1/4 of that. Figure 2.9 depicts this fact. A direct result of the signal footprint differences is the need for different numbers of satellites in order to provide global coverage at all times. As previously mentioned, the GPS constellation requires a minimum of 24 active satellites in order to stay fully operational. Depending on the intended use of a particular LEO constellation (navigation, communication, broadband Internet, etc.), the number of needed satellites can be upwards of three times that of GPS to provide global coverage. While there are significantly fewer GPS satellites in orbit, it costs more to launch the satellites. The higher launch costs also drive manufacturing prices up since GPS satellites need to be made as resilient as possible so as replacements are rarely necessary. This is a benefit of LEO constellations – the launch costs

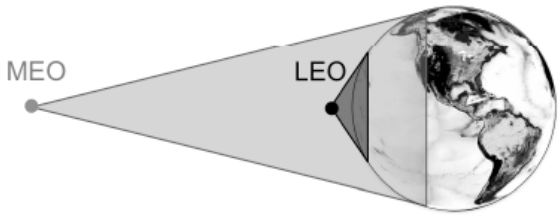

Figure 2.9. MEO vs. LEO signal footprint [39]

are significantly lower, meaning that defective satellites can be easily replaced and manufacturing costs can be kept lower.

A drawback of the lower manufacturing costs, and the simple fact that the majority of LEO constellations weren't designed for navigation purposes, is the absence of high quality clocks and accurate ephemerides. As discussed in Section 2.3, GPS satellites have several atomic clocks on-board to help provide nanosecond level timing accuracy. The size, weight, power, and cost (SWaP-C) of high quality atomic clocks make them unsuitable for LEO satellites. GPS satellites also broadcast detailed and accurate navigation messages, which are monitored and updated by the Control segment, to users. While certain LEO constellations do broadcast navigation messages, as detailed below, others currently do not.

One orbital characteristic working in the favor of LEO constellations, with respect to this particular navigation method, is the speed at which they travel. LEO satellites travel at speeds between 25,600-28,000 km/hr while GPS satellites travel at approximately 14,000 km/hr. The greater relative speed between the user and satellite results in a stronger and more robust Doppler shift observable. Also due to the higher relative speed, multipath effects occur at a much higher rate and therefore tend to average out over intervals of several seconds. For MEO, multipath effects linger for intervals on the order of tens to hundreds of seconds.

The small signal footprint provided from LEO satellites also means that a number of different inclinations will be necessary in order for the constellation to provide global coverage. Because of the altitude of GPS satellites and the signal footprint they provide, only 6 planes at an inclination of 55 degrees are needed to cover the globe – including the poles. LEO constellations either require a large number of planes at an inclination near 90 degrees, or they need to have several planes at a diverse set of inclinations. Chapter 3 will further expand upon the orbital design of

the LEO constellations of interest in this thesis.

2.8.2 TRANSIT

Under sponsorship from the United States Navy, the Johns Hopkins Applied Physics Laboratory (APL) and the Defense Advanced Research Projects Agency (DARPA) jointly developed the Transit System, which was the first satellite navigation system. The first Transit launch was in 1959 and the last was in 1988, with the service operational until 1996 – 3 years after GPS became fully operational. Users could derive their location from the Transit system by precisely knowing the satellite's position and using Doppler shift. Transit satellites transmitted two ultra high frequency (UHF) carrier signals containing time tags and its orbital information. Similar to GPS, Navy ground stations uploaded corrections to the clocks and orbital parameters twice per day [15].

Satellites were launched into low Earth polar orbits at an altitude of approximately 1,100 km. They traveled at roughly 27,000 km/hr with an orbital period of about 106 minutes. Five satellites were necessary to provide reasonable global coverage, while ten satellites were active on average during full operation. The Transit system provided location accuracy of approximately 200 meters for a user tracking a single pass of a satellite. The few satellites in service and the small visibility window for the satellites meant that users were often left without a fix for upwards of an hour, depending on their location. While this fact would make Transit unsuitable for traditional GPS users, it was sufficient for slow moving ships or submarines which could more easily dead reckon during outages [10].

2.8.3 Orbcomm

Orbital Sciences Corporation created the Orbcomm low earth orbit system in the late 1980's to provide global communication and messaging services. Orbital Sciences filed the world's first license application with the Federal Communications Commission (FCC) in 1990, for a network of LEO satellites [17]. Filing an application with the FCC has since become the important first step for any company looking to launch any sort of LEO constellation. Orbital Sciences' successful FCC application allows Orbcomm to operate in the 137-150 Megahertz (MHz) very high frequency (VHF) band. A total of 60 Orbcomm satellites have been launched since 1991, with 59 still in orbit and 35 satellites still operational today. While navigation was not the intended function of the Orbcomm system, there have been studies conducted where users were able to extract pseudorange and Doppler shift observables from the signal, as discussed in Chapter 1.

2.8.4 Iridium

The Iridium satellite constellation was designed in the 1990's, by Iridium Communications, to provide voice and data messaging services to handheld phones. The intention was for handheld devices to communicate with geostationary satellites (35,785 km), however the handheld devices did not have sufficient power to reach such altitudes. To solve this issue, the initial Iridium constellation, launched between 1997-2002, was launched into low Earth orbit at roughly 780 km. The original constellation has since been replaced with the Iridium NEXT constellation, which provided additional capabilities [18]. Iridium NEXT satellites were launched between 2017-2019. The current constellation consists of 66 operational satellites (plus 9 spares) in 6 planes at the same 780 km altitude. The constellation operates in near polar orbits (86.4 degrees) and transmits signals at an L-band frequency of 1,618.85-1,626.5 MHz.

Iridium is another constellation that was not designed for navigation at its inception, but has been utilized for just that.

Satelles, Inc. is a technology company that partners with Iridium Communications to provide position and timing solutions using signals from the Iridium constellation. Iridium transmits a satellite time and location service for use by Satelles to generate accurate PVT. Similar to GPS, this time and location service transmits messages whose accuracies are monitored and updated from the ground. The Satelles LEO navigation solution reaps the benefits described in Section 2.6.1 to augment GPS when it is degraded or denied. An added benefit of the Satelles solution is its operation in the L-band – the same as GPS. This allows Satelles receiver designs to be similar to GPS receivers. An assured positioning, navigation, and timing system leveraging both GPS and Iridium signals could also potentially use the same antenna because both signals reside in the L-band. The Iridium constellation and its use for LEO based navigation is further discussed in Section 3.1.

2.8.5 Future LEO

The Transit, Orbcomm, and Iridium systems give a glimpse at what LEO constellations have historically looked like and been used for. LEO constellations have been larger in satellite number than GPS but not exorbitantly so. In recent years however, several tech companies have filed applications with the FCC to launch large LEO constellations. Many of these large LEO constellations have a common goal of providing global satellite Internet broadband services. OneWeb, a London based communications company, has launched 358 of its satellites into low earth orbit since 2019. SpaceX has successfully launched 1,732 of its Starlink satellites since the start of 2018. Amazon, with its Kuiper constellation, and Canadian communications company Telesat, have also filed FCC applications for large low Earth constellations.

Based on the FCC filings and contingent on successful launches, there could be upwards of 50,000 satellites in LEO in the next 10 years [14]. Even though the majority of these constellations are being launched for purposes other than navigation, there remains a tremendous opportunity to leverage their signals in manners described in this thesis.

2.9 Summary

This chapter described the mathematical notation that will be used throughout this thesis and introduced concepts that will be used. A brief introduction to navigation, as well as traditional GPS, was provided. The difference between low Earth and medium Earth orbit was explored along with the differences between LEO constellations and GPS. Historical and future LEO constellations were covered, some of which will be explored further in Chapter 3. With Chapter 1 and 2 forming a knowledge base, the design and methodology of this research is presented in the following chapter.

3. Design and Methodology

This chapter describes the experimental methodology employed in the assessment of navigation using carrier Doppler measurements from LEO constellations. Section 3.1 introduces the current and emerging LEO constellations that are used in the navigation simulation. Section 3.2 derives the equations necessary for a receiver to navigate using LEO Doppler observables. Section 3.3 describes the simulation and provides the initial conditions used in each simulation scenario. Finally, Section 3.4 derives the equations needed to conduct a GDOP analysis for each constellation.

3.1 Constellations of Interest

As discussed in Chapter 2, there are characteristics of low Earth orbit that are driving factors in the design of a constellation used for navigation purposes. The typically small coverage area of LEO constellations will require both a large number of satellites, and either a larger number of planes or several different inclinations. This thesis will explore the individual suitability of the Kuiper, OneWeb, Starlink, and Telesat constellations for navigation. Two "constellation of constellations (CoC)" will also be explored. The first will include all of the satellites in orbit from the Iridium NEXT, OneWeb, and Starlink constellations as of April 8th, 2021. The second will include all of the satellites in the planned Kuiper, OneWeb, Starlink, and Telesat constellations. The public FCC filings, when available, were used to design the constellations and this information was also used to fabricate the necessary TLE files.

3.1.1 Kuiper

Amazon has filed an application with the FCC for a constellation of 3,236 satellites operating at altitudes between 590-630 kilometers [21]. The satellite-to-user signal is planned to be transmitted at frequencies of 17.7 - 20.2 Gigahertz (GHz). To date, there have been no satellites launched, with the first launches schedule in 2022. Table 3.1 presents the anticipated design of the Kuiper constellation. The number

Table 3.1. Kuiper Constellation

Satellites	Altitude [km]	Inclination [deg]	Planes	SV's Per Plane
784	590	33.0	34	34
1,296	610	42.0	36	36
1,156	630	51.9	28	28

of planned satellites in the Kuiper constellation make it an appealing option for navigation purposes. However, the fact that all satellites have inclinations between 33-51.9 degrees mean that the satellite coverage will be very poor at higher and lower latitudes and nonexistent at the poles. Additional satellites would need to be launched at inclinations closer to 90 degrees, or another constellation would need to be leveraged in order for the Kuiper constellation to provide the necessary global coverage.

3.1.2 OneWeb

OneWeb has plans to launch a constellation of 6,372 satellites at an altitude of 1,200 kilometers [22]. To date, the company has successfully launched 348 satellites with the first being launched in February, 2019. The constellation's satellite-to-user signal operates at 40.0-42.0 GHz. Table 3.2 shows the design of the complete OneWeb constellation. Similar to the Kuiper constellation, OneWeb has plans for a large number of satellites in LEO that make it an obvious choice for this research. Unlike

Table 3.2. OneWeb Constellation

Satellites	Altitude [km]	Inclination [deg]	Planes	SV's Per Plane
1,764	1200	87.9	36	49
2,304	1200	55.0	32	72
2,304	1200	40.0	32	72

Kuiper, the OneWeb constellation has satellites at inclinations of 40.0, 55.0, and 87.9 degrees. The volume of satellites at each of these inclinations also mean that OneWeb should be able to provide sufficient global coverage at all times.

3.1.3 Starlink

SpaceX has filed several applications with the FCC for a LEO constellation consisting of 11,914 vehicles operating at altitudes between 335-570 kilometers. While the original design had satellites at altitudes up to 1200 kilometers, the FCC approved a modification from SpaceX to keep all satellites below 570 kilometers [19]. The satellite-to-user signal from Starlink satellites is transmitted at 10.7-12.7 GHz. Table 3.3 shows the design of the full Starlink constellation, proposed to be complete by November, 2027. Please note that the values with an asterisk have not been determined by SpaceX as of yet. The number of planes and satellites per plane were chosen here to achieve the intended number of satellites in the fully operational constellation. Also note that an inclination between 90-180 degrees constitutes a retrograde orbit, while an inclination between 0-90 degrees is a prograde orbit. A prograde orbit rotates in the same direction of the Earth and a retrograde orbit rotates in the opposite direction. Similar to OneWeb, the Starlink constellation has a significant number of satellites at a wide range of inclinations. The massive number of satellites at inclinations between 42-70 degrees will undoubtedly provide more than enough signal coverage in the mid-latitude regions. Even though the Starlink plans call for 508 satellites in near polar orbit, it may not provide enough coverage around the poles

Table 3.3. Starlink Constellation

Satellites	Altitude [km]	Inclination [deg]	Planes	SV's Per Plane
1,584	550	53.0	72	22
1,584	584	53.2	72	22
720	570	70.0	36	20
172	560	97.6	4	43
336	560	97.6	6	58
2,493	335.9	42.0	28*	89*
2,478	340.8	48.0	42*	59*
2,547	345.6	53.0	49*	52*

at all times.

3.1.4 Telesat

Telesat is another communications company that has filed applications with the FCC for a constellation of LEO satellites [20]. Telesat's constellation is comprised of 298 satellites at altitudes of 1015 and 1325 kilometers. The satellite-to-user signal is transmitted at a frequency of 37.5-40 GHz. Several test satellites have been launched since 2018 by Telesat, with the rest of the constellation scheduled for launch in the coming years. Table 3.4 shows the design of the Telesat constellation. Compared

Table 3.4. Telesat Constellation

Satellites	Altitude [km]	Inclination [deg]	Planes	SV's Per Plane
78	1015	88.0	6	13
220	1325	45.0	20	11

to the other large LEO constellations discussed here, Telesat is by far the smallest in number. The inclination diversity of the satellites is the reason the Telesat constellation was considered in this research. Coverage gaps are to be expected with a constellation of this size when at least 8 are necessary for navigation. Section 3.2.1 explains the need for 8 satellites when pseudorange-based navigation only requires 4.

The Telesat constellation can still provide value in a multi-constellation solution by improving coverage at the poles and improving overall user-satellite geometry.

3.1.5 Current Constellation of Constellations

As mentioned above, the first multi-constellation solution that is explored includes the Iridium NEXT, OneWeb, and Starlink constellations as of April 8th, 2021. These constellations are considered for a number of reasons. The Iridium constellation is one of the most mature LEO constellations and is already leveraged for navigation purposes. OneWeb and Starlink both represent the mega LEO constellations that will be launched in the coming years and they are the only two that currently have a substantial number of satellites in orbit. The differing altitudes and inclinations between constellations also provide better potential for global coverage and favorable satellite geometry for navigation applications. Table 3.5 shows the state of all 3 constellations as of April 8th, 2021. The Starlink constellation includes satellites

Table 3.5. Iridium NEXT, OneWeb, and Starlink Constellations as of April 8th, 2021

Constellation	**Satellites**	**Altitude [km]**	**Inclination [deg]**
Iridium NEXT	75	780	86.4
OneWeb	146	1200	87.9
Starlink	1279	550	53.0
	10	560	97.6

at an inclination of 53 degrees which helps to provide coverage in the mid-latitude regions. The Iridium NEXT and OneWeb constellations include satellites in near polar orbits that will provide coverage around the poles. As the OneWeb and Starlink constellations grow, the signal coverage and user-satellite geometry will continue to improve.

3.1.6 Future Constellation of Constellations

The second multi-constellation solution researched includes the planned fully operational constellations of Kuiper, OneWeb, Starlink, and Telesat. The idea behind including these constellations was to explore the kind of global coverage and satellite geometry that could be achieved using several mega-constellations with differing altitudes and inclinations. For comparison's sake, the 4 constellation designs are included in Table 3.6. Each of the 4 constellations provide lower and mid-inclination

Table 3.6. Planned Kuiper, OneWeb, Starlink, and Telesat Constellations

Constellation	Satellites	Alt. [km]	Inc. [deg]	Planes	SV's Per Plane
Kuiper	784	590	33.0	34	34
	1,296	610	42.0	36	36
	1,156	630	51.9	28	28
OneWeb	1,764	1200	87.9	36	49
	2,304	1200	55.0	32	72
	2,304	1200	40.0	32	72
Starlink	1,584	550	53.0	72	22
	1,584	584	53.2	72	22
	720	570	70.0	36	20
	172	560	97.6	4	43
	336	560	97.6	6	58
	2,493	335.9	42.0	28*	89*
	2,478	340.8	48.0	42*	59*
	2,547	345.6	53.0	49*	52*
Telesat	78	1015	88.0	6	13
	220	1325	45.0	20	11

satellites, while the OneWeb, Starlink, and Telesat constellations provide the near 90 degree inclination satellites. The 21,820 satellites in this mega-constellation make it an order of magnitude larger than any single constellation in orbit, especially those used for navigation. One potential design consideration, which is not included in this research, is signal deconfliction. A single receiver might struggle to differentiate the signals from potentially thousands of satellites. However, A constellation of this size

is included in this research to demonstrate the type of navigation performance that it might result in.

3.2 Point-Solution Batch Filter

The measured carrier Doppler shift from a given satellite is equal to the negative time derivative of the accumulated delta range, divided by the wavelength of the transmitted signal.

$$D^j = -\frac{1}{\lambda}\frac{d\Delta\rho^j_{ADR}}{dt_R} \tag{3.1}$$

Psiaki develops a point solution algorithm to simultaneously solve for position, velocity, clock offset, and clock offset rate using the carrier Doppler shift from 8 satellites in [38]. The navigation solution is estimated by solving the following nonlinear least-squares problem, where position ($\vec{r}$), clock offset (δ_R), velocity ($\vec{v}$), and clock offset rate ($\dot{\delta}_R$) are found in order to minimize the cost function:

$$J(\vec{r},\delta_R,\vec{v},\dot{\delta}_R) = \frac{1}{2}\sum_{j=1}^{N}\left[\frac{\lambda D^j + \frac{d\Delta\rho^j_{ADR}}{dt_R}\Big|_{(\vec{r},\delta_R,\vec{v},\dot{\delta}_R)}}{\lambda\sigma^j_{Dopp}}\right]^2 \tag{3.2}$$

The term on the right hand side of the numerator in Equation 3.2 is the accumulated delta range rate, and is solved for below. The denominator term, $\lambda\sigma^j_{Dopp}$, is the range-rate-equivalent measurement error standard deviation for the j^{th} satellite. λ is the carrier wavelength of the signal in meters, and D^j is the Doppler shift from the j^{th} satellite. Minimization of $J(\vec{r},\delta_R,\vec{v},\dot{\delta}_R)$ leads to an estimation of receiver position, clock offset, velocity, and clock offset rate.

3.2.1 Accumulated Delta Range

Before the accumulated delta range rate can be found, the accumulated delta range must first be solved for.

$$\begin{aligned}\Delta\rho^j_{ADR}(\vec{r},\delta_R;t_R) =&\sqrt{[\vec{r}-\mathbf{A}(\omega_E\delta t^j_p)\vec{r}^j(t_R-\delta_R-\delta t^j_p)]^\top[\vec{r}-\mathbf{A}(\omega_E\delta t^j_p)\vec{r}^j(t_R-\delta_R-\delta t^j_p)]}\\ &+c(\delta_R-\delta^j)+c(\delta^j_{trop}-\delta^j_{iono})+\lambda\beta \end{aligned} \tag{3.3}$$

In Equation 3.3, $\vec{r}$ is the unknown receiver position in ECEF coordinates, $\vec{r}^j$ is the known position of the j^{th} satellite in ECEF coordinates, ω_E is the rotation rate of the Earth, δt^j_p is the signal propagation time from the satellite to the receiver, δ^j is the satellite clock offset, δ^j_{trop} is the signal delay due to the troposphere, δ^j_{iono} is the signal delay due to the ionosphere, β is the beat carrier phase, and t_R is the erroneous receiver clock time. The signal propagation time is found using Equation 3.4.

$$\begin{aligned}\delta t^j_p =&\sqrt{[\vec{r}-\mathbf{A}(\omega_E\delta t^j_p)\vec{r}^j(t_R-\delta_R-\delta t^j_p)]^\top[\vec{r}-\mathbf{A}(\omega_E\delta t^j_p)\vec{r}^j(t_R-\delta_R-\delta t^j_p)]}\\ &+\delta^j_{trop}-\delta^j_{iono}\end{aligned} \tag{3.4}$$

In order to compensate for the rotation of the ECEF coordinate frame while the signal is traveling to the receiver, the satellite position is multiplied by a direction cosine matrix, $\mathbf{A}(\omega_E\delta t^j_p)$.

$$A(\omega_E\delta t^j_p) = \begin{bmatrix}\cos(\omega_E\delta t^j_p) & \sin(\omega_E\delta t^j_p) & 0\\ -\sin(\omega_E\delta t^j_p) & \cos(\omega_E\delta t^j_p) & 0\\ 0 & 0 & 1\end{bmatrix} \tag{3.5}$$

Methods for calculating the tropospheric and ionospheric delays are detailed in [40]. With equations to calculate the accumulated delta range between a receiver and a given satellite, the accumulated delta range rate can now be derived. Psiaki presents

a 5-point finite difference formula that numerically computes the time derivative of the accumulated delta range.

$$\left.\frac{d\Delta\rho^j_{ADR}}{dt_R}\right|_{(\vec{r},\delta_R,\vec{v},\dot{\delta}_R)} = \{\Delta\rho^j_{ADR}(\vec{r} - \frac{2\vec{v}\Delta t_R}{1+\dot{\delta}_R}, \delta_R - \frac{2\dot{\delta}_R\Delta t_R}{1+\dot{\delta}_R}; t_R - 2\Delta t_R)$$
$$-8\Delta\rho^j_{ADR}(\vec{r} - \frac{\vec{v}\Delta t_R}{1+\dot{\delta}_R}, \delta_R - \frac{\dot{\delta}_R\Delta t_R}{1+\dot{\delta}_R}; t_R - \Delta t_R)$$
$$+8\Delta\rho^j_{ADR}(\vec{r} + \frac{\vec{v}\Delta t_R}{1+\dot{\delta}_R}, \delta_R + \frac{\dot{\delta}_R\Delta t_R}{1+\dot{\delta}_R}; t_R + \Delta t_R)$$
$$-\Delta\rho^j_{ADR}(\vec{r} + \frac{2\vec{v}\Delta t_R}{1+\dot{\delta}_R}, \delta_R + \frac{2\dot{\delta}_R\Delta t_R}{1+\dot{\delta}_R}; t_R + 2\Delta t_R)\}\frac{1}{12\Delta t_R} \quad (3.6)$$

Δt_R is the nominal finite difference interval of the erroneous receiver clock time, which Psiaki recommends setting between 0.1 sec $\leq \Delta t_R \leq$ 0.25 sec – this research uses a value of $\Delta t_R = 0.175$ sec. Please note that Equation 3.6 only contains 4 terms because of the zero-weighting placed on the middle term. The accumulated delta range rate from Equation 3.6 is substituted into the cost function in Equation 2.1, which is used to solve for position, clock offset, velocity, and clock offset rate.

Equation 3.6 illustrates why Doppler measurements are needed from 8 satellites in order for a receiver to derive position and time. In a traditional pseduorange-based navigation system where an equation similar to Equation 2.9 is used, a receiver is only solving for 4 unknowns. By simultaneously tracking 4 satellites, a receiver can solve for its three dimensional position and time. However, Equation 3.6 contains 8 unknowns – three dimensional position, clock offset, three dimensional velocity, and clock offset rate. Therefore, a receiver using the method detailed in this research needs Doppler measurements from 8 satellites in order to navigate.

3.2.2 Batch Least-Squares Filter

The cost function in Equation 2.1 can be modified into the standard weighted nonlinear least-squares form, shown in Equation 3.7:

$$J(\vec{x}) = \frac{1}{2}[\vec{y} - \vec{h}(\vec{x})]^{\top}\mathbf{R}^{-1}[\vec{y} - \vec{h}(\vec{x})], \tag{3.7}$$

where $\vec{x}$ is the 8 x 1 vector of unknown receiver quantities being estimated,

$$\vec{x} = \begin{bmatrix} \vec{r} \\ \delta_R \\ \vec{v} \\ \dot{\delta}_R \end{bmatrix} = \begin{bmatrix} r_x \\ r_y \\ r_z \\ \delta_R \\ v_x \\ v_y \\ v_z \\ \dot{\delta}_R \end{bmatrix},$$

$\vec{y}$ is the N x 1 measurement vector,

$$\vec{y} = \begin{bmatrix} \lambda D^1 \\ \lambda D^2 \\ \lambda D^3 \\ \vdots \\ \lambda D^N \end{bmatrix},$$

$\vec{h}(\vec{x})$ is the N x 1 nonlinear measurement model function,

$$\vec{h}(\vec{x}) = \begin{bmatrix} \frac{d\Delta\rho^1_{ADR}}{dt_R}\Big|_{(\vec{r},\delta_R,\vec{v},\dot{\delta}_R)} \\ \frac{d\Delta\rho^2_{ADR}}{dt_R}\Big|_{(\vec{r},\delta_R,\vec{v},\dot{\delta}_R)} \\ \frac{d\Delta\rho^3_{ADR}}{dt_R}\Big|_{(\vec{r},\delta_R,\vec{v},\dot{\delta}_R)} \\ \vdots \\ \frac{d\Delta\rho^N_{ADR}}{dt_R}\Big|_{(\vec{r},\delta_R,\vec{v},\dot{\delta}_R)} \end{bmatrix},$$

and $\mathbf{R}$ is the N x N measurement error covariance matrix,

$$\mathbf{R} = \begin{bmatrix} (\lambda\sigma^1_{Dopp})^2 & 0 & 0 & \dots & 0 \\ 0 & (\lambda\sigma^2_{Dopp})^2 & 0 & \dots & 0 \\ 0 & 0 & (\lambda\sigma^3_{Dopp})^2 & \dots & 0 \\ \vdots & \vdots & \vdots & \ddots & \vdots \\ 0 & 0 & 0 & \dots & (\lambda\sigma^N_{Dopp})^2 \end{bmatrix}$$

In order to solve this nonlinear least-squares problem, the Gauss-Newton method will be applied. The nonlinear problem is linearized by calculating the Jacobian matrix of the nonlinear measurement model function. This involves taking the partial derivative of the function with respect to each of the variables in the state vector, $\vec{x}$.

3.2.3 Jacobian Derivation

$$\mathbf{H} = \frac{\partial}{\partial \vec{x}}\vec{h}(\vec{x}) = \begin{bmatrix} \frac{\partial \vec{h}^1(\vec{x})}{\partial r_x} & \frac{\partial \vec{h}^1(\vec{x})}{\partial r_y} & \frac{\partial \vec{h}^1(\vec{x})}{\partial r_z} & \frac{\partial \vec{h}^1(\vec{x})}{\partial \delta_R} & \frac{\partial \vec{h}^1(\vec{x})}{\partial v_x} & \frac{\partial \vec{h}^1(\vec{x})}{\partial v_y} & \frac{\partial \vec{h}^1(\vec{x})}{\partial v_z} & \frac{\partial \vec{h}^1(\vec{x})}{\partial \dot{\delta}_R} \\ \frac{\partial \vec{h}^2(\vec{x})}{\partial r_x} & \frac{\partial \vec{h}^2(\vec{x})}{\partial r_y} & \frac{\partial \vec{h}^2(\vec{x})}{\partial r_z} & \frac{\partial \vec{h}^2(\vec{x})}{\partial \delta_R} & \frac{\partial \vec{h}^2(\vec{x})}{\partial v_x} & \frac{\partial \vec{h}^2(\vec{x})}{\partial v_y} & \frac{\partial \vec{h}^2(\vec{x})}{\partial v_z} & \frac{\partial \vec{h}^2(\vec{x})}{\partial \dot{\delta}_R} \\ \frac{\partial \vec{h}^3(\vec{x})}{\partial r_x} & \frac{\partial \vec{h}^3(\vec{x})}{\partial r_y} & \frac{\partial \vec{h}^3(\vec{x})}{\partial r_z} & \frac{\partial \vec{h}^3(\vec{x})}{\partial \delta_R} & \frac{\partial \vec{h}^3(\vec{x})}{\partial v_x} & \frac{\partial \vec{h}^3(\vec{x})}{\partial v_y} & \frac{\partial \vec{h}^3(\vec{x})}{\partial v_z} & \frac{\partial \vec{h}^3(\vec{x})}{\partial \dot{\delta}_R} \\ \vdots & \vdots & \vdots & \vdots & \vdots & \vdots & \vdots & \vdots \\ \frac{\partial \vec{h}^N(\vec{x})}{\partial r_x} & \frac{\partial \vec{h}^N(\vec{x})}{\partial r_y} & \frac{\partial \vec{h}^N(\vec{x})}{\partial r_z} & \frac{\partial \vec{h}^N(\vec{x})}{\partial \delta_R} & \frac{\partial \vec{h}^N(\vec{x})}{\partial v_x} & \frac{\partial \vec{h}^N(\vec{x})}{\partial v_y} & \frac{\partial \vec{h}^N(\vec{x})}{\partial v_z} & \frac{\partial \vec{h}^N(\vec{x})}{\partial \dot{\delta}_R} \end{bmatrix} \tag{3.8}$$

The full Jacobian matrix requires partial derivatives of each of the 4 terms in Equation 3.6 with respect to each receiver unknown. For the purposes of this document, only the partial derivatives of the first term in Equation 3.6 will be presented, but the process is the same for the remaining 3 terms. In order to make the equations more reader friendly, some abbreviations will be explicitly defined and used below. The square root term from Equation 3.3 will be abbreviated as $\sqrt{\vec{\theta}^\top\vec{\theta}}$, where

$$\sqrt{\vec{\theta}^\top\vec{\theta}} = \sqrt{[\vec{r} - \mathbf{A}(\omega_E\delta t^j_p)\vec{r}^j(t_R - \delta_R - \delta t^j_p)]^\top[\vec{r} - \mathbf{A}(\omega_E\delta t^j_p)\vec{r}^j(t_R - \delta_R - \delta t^j_p)]}.$$

The partial derivative with respect to the receiver's ECEF x-position, r_x, is derived below. The terms in parenthesis are plugged in as $\vec{r}$, δ_R, and Δt_R in Equation 3.3, respectively.

$$\frac{\partial}{\partial r_x}\Delta\rho^j_{ADR}(\vec{r}-\frac{2\vec{v}\Delta t_R}{1+\dot{\delta}_R},\delta_R-\frac{2\dot{\delta}_R\Delta t_R}{1+\dot{\delta}_R};t_R-2\Delta t_R)$$
$$=\frac{\partial}{\partial r_x}\left(\sqrt{\vec{\theta}^\top\vec{\theta}}+c(\delta_R-\delta^j)+c(\delta^j_{trop}-\delta^j_{iono})+\lambda\beta\right)$$

Because $\vec{r}$ appears in the signal propagation delay term, δ^j_{tp}, we will need to find the partial derivative of $\mathbf{A}(\omega_E\delta t^j_p)$ and $\vec{r}^j(t_R-\delta_R-\delta t^j_p)$ with respect to r_x.

$$\frac{\partial}{\partial r_x}\mathbf{A}(\omega_E\delta t^j_p)=\mathbf{A}'_x$$

$$\mathbf{A}'_x=\frac{\omega_E}{c}\frac{r_x-(\cos(\omega_E\delta t^j_p)r^j_x+\sin(\omega_E\delta t^j_p)r^j_y)}{\sqrt{\vec{\theta}^\top\vec{\theta}}}\begin{bmatrix}-\sin(\omega_E\delta t^j_p) & \cos(\omega_E\delta t^j_p) & 0\end{bmatrix} \quad (3.9)$$

$$\frac{\partial}{\partial r_x}\vec{r}^j(t_R-\delta_R-\delta t^j_p)=r^{j'}_x$$

$$r^{j'}_x=-\frac{1}{c}\frac{r_x-(\cos(\omega_E\delta t^j_p)r^j_x+\sin(\omega_E\delta t^j_p)r^j_y)}{\sqrt{\vec{\theta}^\top\vec{\theta}}}v^j_x(t_R-\delta_R-\delta t^j_p) \quad (3.10)$$

r_x is the x-component of $\vec{r}-\frac{2\vec{v}\Delta t_R}{1+\dot{\delta}_R}$, r^j_x and r^j_y are the x- and y-components of the satellite position vector, respectively, and v^j_x is the x-component of the satellite velocity vector. Because this process will be repeated for the partial derivatives with respect to r_y and r_z, the terms $r^{j'}_y$, $r^{j'}_z$, and $\mathbf{A}'_y$ are also derived below.

$$\frac{\partial}{\partial r_y}\mathbf{A}(\omega_E\delta^j_{tp})=\mathbf{A}'_y$$

$$\mathbf{A}'_y=\frac{\omega_E}{c}\frac{r_y-(-\sin(\omega_E\delta^j_{tp})r^j_x+\cos(\omega_E\delta^j_{tp})r^j_y)}{\sqrt{\vec{\theta}^\top\vec{\theta}}}\begin{bmatrix}-\cos(\omega_E\delta^j_{tp}) & -\sin(\omega_E\delta^j_{tp}) & 0\end{bmatrix} \quad (3.11)$$

$$\frac{\partial}{\partial r_y}\vec{r^j}(t_R - \delta_R - \delta t_p^j) = r_y^{j'}$$

$$r_y^{j'} = -\frac{1}{c}\frac{r_y - (-\sin(\omega_E \delta t_p^j) r_x^j + \cos(\omega_E \delta t_p^j) r_y^j)}{\sqrt{\vec{\theta}^\top \vec{\theta}}} v_y^j (t_R - \delta_R - \delta t_p^j) \tag{3.12}$$

$$\frac{\partial}{\partial r_z}\vec{r^j}(t_R - \delta_R - \delta t_p^j) = r_z^{j'}$$

$$r_z^{j'} = -\frac{1}{c}\frac{r_z - r_z^j}{\sqrt{\vec{\theta}^\top \vec{\theta}}} v_z^j (t_R - \delta_R - \delta t_p^j) \tag{3.13}$$

Note that because the bottom row of the direction cosine matrix, $\mathbf{A}(\omega_E \delta t_P^j)$, consists of only zeros, the partial derivative with respect to r_z is 0. $\vec{r^{j'}}$ can also be constructed using the partial derivatives in Equations 3.10, 3.12, and 3.13.

$$\vec{r^{j'}} = \begin{bmatrix} r_x^{j'} \\ r_y^{j'} \\ r_z^{j'} \end{bmatrix} \tag{3.14}$$

With the terms in Equations 3.9 - 3.14, analytical expressions for the partial derivatives with respect to r_x, r_y, and r_z are defined below.

$$\frac{\partial}{\partial r_x}\Delta\rho_{ADR}^j(\vec{r} - \frac{2\vec{v}\Delta t_R}{1+\dot{\delta}_R}, \delta_R - \frac{2\dot{\delta}_R \Delta t_R}{1+\dot{\delta}_R}; t_R - 2\Delta t_R) =$$
$$\frac{r_x - (\mathbf{A}_x \vec{r^j} + (\mathbf{A}'_x \vec{r^j} + \mathbf{A}_x \vec{r^{j'}}) r_x) - \frac{1}{2}(\mathbf{A}'_x \vec{r^j} \mathbf{A}_x \vec{r^j} + (r_x^{j'} \mathbf{A}_x \vec{r^j} + (\mathbf{A}'_x \vec{r^j} + \mathbf{A}_x \vec{r^{j'}}) \vec{r^j}) \mathbf{A}_x)}{\sqrt{\vec{\theta}^\top \vec{\theta}}} \tag{3.15}$$

$$\frac{\partial}{\partial r_y}\Delta\rho_{ADR}^j(\vec{r} - \frac{2\vec{v}\Delta t_R}{1+\dot{\delta}_R}, \delta_R - \frac{2\dot{\delta}_R \Delta t_R}{1+\dot{\delta}_R}; t_R - 2\Delta t_R) =$$
$$\frac{r_y - (\mathbf{A}_y \vec{r^j} + (\mathbf{A}'_y \vec{r^j} + \mathbf{A}_y \vec{r^{j'}}) r_y) - \frac{1}{2}(\mathbf{A}'_y \vec{r^j} \mathbf{A}_y \vec{r^j} + (r_y^{j'} \mathbf{A}_y \vec{r^j} + (\mathbf{A}'_y \vec{r^j} + \mathbf{A}_y \vec{r^{j'}}) \vec{r^j}) \mathbf{A}_y)}{\sqrt{\vec{\theta}^\top \vec{\theta}}} \tag{3.16}$$

$$\frac{\partial}{\partial r_z}\Delta\rho^j_{ADR}(\vec{r}-\frac{2\vec{v}\Delta t_R}{1+\dot{\delta}_R},\delta_R-\frac{2\dot{\delta}_R\Delta t_R}{1+\dot{\delta}_R};t_R-2\Delta t_R)= \\ \frac{r_z-(r^j_z+r^{j'}_z r_z)-r^{j'}_z r^j_z}{\sqrt{\vec{\theta}^\top\vec{\theta}}} \tag{3.17}$$

In Equations 3.15 and 3.16, $\mathbf{A}_x$ and $\mathbf{A}_y$ denote the first and second rows of the direction cosine matrix, respectively, from Equation 3.5.

The next partial derivative needed is with respect to the receiver clock offset. Similar to with the receiver position partial derivatives, δ_R appears in the $\vec{r}^j(t_R-\delta_R-\delta t^j_p)$ term.

$$\frac{\partial}{\partial\delta_R}\vec{r}^j(t_R-\delta_R-\delta t^j_p)=\vec{r}^{j'}_{\delta_R}$$

$$\vec{r}^{j'}_{\delta_R}=-\vec{v}^j(t_R-\delta_R-\delta t^j_p), \tag{3.18}$$

where $\vec{v}$ is the known satellite velocity vector. Using Equation 3.18 the full partial derivative with respect to clock offset can be derived.

$$\frac{\partial}{\partial\delta_R}\Delta\rho^j_{ADR}(\vec{r}-\frac{2\vec{v}\Delta t_R}{1+\dot{\delta}_R},\delta_R-\frac{2\dot{\delta}_R\Delta t_R}{1+\dot{\delta}_R};t_R-2\Delta t_R)= \\ \frac{\vec{r}^j\mathbf{A}(\omega_E\delta t^j_p)\vec{r}^{j'}_{\delta_R}-\mathbf{A}(\omega_E\delta t^j_p)\vec{r}\mathbf{A}(\omega_E\delta t^j_p)\vec{r}^{j'}_{\delta_R}}{\sqrt{\vec{\theta}^\top\vec{\theta}}}+c \tag{3.19}$$

The partial derivatives with respect to the receiver velocity components are similar to those with respect to the position components. In fact, the velocity partial derivatives can be calculated by scaling the position partial derivatives by $\frac{\partial}{\partial\vec{v}}\left(\vec{r}-\frac{2\vec{v}\Delta t_R}{1+\dot{\delta}_R}\right)$.

$$\frac{\partial}{\partial\vec{v}}\left(\vec{r}-\frac{2\vec{v}\Delta t_R}{1+\dot{\delta}_R}\right)=-\frac{2\Delta t_R}{1+\dot{\delta}_R}$$

$$\frac{\partial}{\partial v_x}\Delta\rho^j_{ADR}(\vec{r}-\frac{2\vec{v}\Delta t_R}{1+\dot{\delta}_R},\delta_R-\frac{2\dot{\delta}_R\Delta t_R}{1+\dot{\delta}_R};t_R-2\Delta t_R)=-\frac{2\Delta t_R}{1+\dot{\delta}_R}\left(\frac{\partial}{\partial r_x}\Delta\rho^j_{ADR}(...)\right) \tag{3.20}$$

$$\frac{\partial}{\partial v_y}\Delta\rho^j_{ADR}(\vec{r}-\frac{2\vec{v}\Delta t_R}{1+\dot{\delta}_R},\delta_R-\frac{2\dot{\delta}_R\Delta t_R}{1+\dot{\delta}_R};t_R-2\Delta t_R)=-\frac{2\Delta t_R}{1+\dot{\delta}_R}\left(\frac{\partial}{\partial r_y}\Delta\rho^j_{ADR}(...)\right) \quad (3.21)$$

$$\frac{\partial}{\partial v_z}\Delta\rho^j_{ADR}(\vec{r}-\frac{2\vec{v}\Delta t_R}{1+\dot{\delta}_R},\delta_R-\frac{2\dot{\delta}_R\Delta t_R}{1+\dot{\delta}_R};t_R-2\Delta t_R)=-\frac{2\Delta t_R}{1+\dot{\delta}_R}\left(\frac{\partial}{\partial r_z}\Delta\rho^j_{ADR}(...)\right) \quad (3.22)$$

Similar to the partial derivatives with respect to $\vec{v}$, the partial derivative with respect to $\dot{\delta}_R$ can be derived by utilizing Equations 3.15, 3.16, 3.17, and 3.19 and scaling them by $\frac{\partial}{\partial\dot{\delta}_R}\left(\vec{r}-\frac{2\vec{v}\Delta t_R}{1+\dot{\delta}_R}\right)$ or $\frac{\partial}{\partial\dot{\delta}_R}\left(\delta_R-\frac{2\dot{\delta}_R\Delta t_R}{1+\dot{\delta}_R}\right)$.

$$\frac{\partial}{\partial\dot{\delta}_R}\left(\vec{r}-\frac{2\vec{v}\Delta t_R}{1+\dot{\delta}_R}\right)=\frac{2\vec{v}\Delta t_R}{(1+\dot{\delta}_R)^2}$$

$$\frac{\partial}{\partial\dot{\delta}_R}\left(\delta_R-\frac{2\dot{\delta}_R\Delta t_R}{1+\dot{\delta}_R}\right)=-\frac{2\Delta t_R}{(1+\dot{\delta}_R)^2}$$

$$\begin{aligned}\frac{\partial}{\partial\dot{\delta}_R}\Delta\rho^j_{ADR}(\vec{r}-\frac{2\vec{v}\Delta t_R}{1+\dot{\delta}_R},\delta_R-\frac{2\dot{\delta}_R\Delta t_R}{1+\dot{\delta}_R};t_R-2\Delta t_R)=&\\ \frac{2v_x\Delta t_R}{(1+\dot{\delta}_R)^2}\left(\frac{\partial}{\partial r_x}\Delta\rho^j_{ADR}(...)\right)+\frac{2v_y\Delta t_R}{(1+\dot{\delta}_R)^2}\left(\frac{\partial}{\partial r_y}\Delta\rho^j_{ADR}(...)\right)&\\ +\frac{2v_z\Delta t_R}{(1+\dot{\delta}_R)^2}\left(\frac{\partial}{\partial r_z}\Delta\rho^j_{ADR}(...)\right)-\frac{2\Delta t_R}{(1+\dot{\delta}_R)^2}\left(\frac{\partial}{\partial\delta_R}\Delta\rho^j_{ADR}(...)\right)&\end{aligned} \quad (3.23)$$

Again, please note that all of the partial derivatives derived in the equations above are only for the first term in Equation 3.6, where:

$$\vec{r}=\vec{r}-\frac{2\vec{v}\Delta t_R}{1+\dot{\delta}_R}$$

$$\delta_R=\delta_R-\frac{2\dot{\delta}_R\Delta t_R}{1+\dot{\delta}_R}$$

$$t_r=t_R-2\Delta t_R$$

To find the full measurement model Jacobian matrix, this process needs to be repeated

for the remaining 3 terms, after which the partial derivatives are summed. With the full Jacobian matrix defined, the Gauss-Newton method from Section 2.2 is utilized to estimate receiver position, clock offset, velocity, and clock offset rate.

3.3 Simulation

A Python simulation was generated to assess the feasibility of a receiver to accurately estimate its PVT when using this carrier Doppler shift navigation method, along with the different constellations mentioned above. In the simulation, both active and fabricated TLE files are used in conjunction with an orbit propagator to provide satellite position and velocity information to the receiver. Any satellite that appears above a 7.5 degree elevation mask from the receiver is assumed to provide a valid carrier Doppler shift observable. The truth location was randomly selected to be anywhere on the Earth with equal probability. The truth altitude was also selected from a uniform distribution between 0 and 5000 meters. The truth receiver clock offset was sampled from a uniform distribution between -0.25 sec and 0.25 sec. The truth receiver velocity was sampled from a Gaussian distribution with a mean of 0 and a standard deviation of 25 m/sec for each of the ECEF directions. Finally, the truth receiver clock offset rates have been sampled from a Gaussian distribution with a mean value of 0 and a standard deviation of 3.336×10^{-9} seconds/second. Though the true range-rate-equivalent measurement error standard deviation is yet to be determined, it is assumed to be in line with that of GPS, $\lambda\sigma^{j}_{Dopp} = 0.01$ m/sec. The true value depends on several factors, including the signal's carrier-to-noise ratio.

3.3.1 Initial Conditions

Table 3.7 provides a summary of the initial conditions of each of the 4 scenarios. Four different test scenarios are considered for each of the constellations of inter-

Table 3.7. Initial Conditions of 4 Different Test Scenarios

	Scenario	**Description**
1a	No cold start, No SV errors	Initial horizontal error between 143-151 km. No satellite ephemeris or timing error.
1b	No cold start, SV errors	Initial horizontal error between 143-151 km. Satellite ephemeris and timing error assumed.
2a	Cold start, No SV errors	Receiver initialized to $\vec{r} = [0, 0, 0]$. No satellite ephemeris or timing error.
2b	Cold start, SV errors	Receiver initialized to $\vec{r} = [0, 0, 0]$. Satellite ephemeris and timing error assumed.

est. The differences between the scenarios are in regard to the initial receiver errors and the assumed accuracy of the ephemerides and timing provided by each satellite. The tropospheric and ionospheric delays calculated by the receiver are assumed to perfectly match the truth values.

Two sets of initial receiver errors are considered, with the first being proposed by Psiaki in [38]. The receiver is initialized with a horizontal position error between 143 and 151 kilometers. The receiver is initialized at an altitude of 0 meters, a velocity of 0 m/sec, a clock offset of 0 seconds, and a clock offset rate of 0 seconds/second. This means that the initial altitude errors form a uniform distribution in the range -5000 and 0 meters. The initial clock offset errors are a uniform distribution as well, in the range from -0.25 to 0.25 seconds. The initial velocity errors in each axis form a Gaussian distribution with a mean of 0 and standard deviation of 25 m/sec. The initial clock offset rate errors form a zero-mean Gaussian distribution with a standard deviation of 3.336×10^{-9} seconds/second. The second set of initial receiver conditions is meant to simulate a true cold start scenario. The receiver is initialized to a latitude and longitude of 0 degrees and an altitude of 0 meters. While different receivers behave differently in the case of a cold start, it is assumed that the receiver defaults to the equator following a cold start. The clock offset is initialized to 0 sec, the velocity is initialized to 0 m/sec, and the clock offset rate is initialized to

0 seconds/second. The initial clock offset, velocity, and clock offset rate errors are distributed identically to those in [38]. The initial position errors, however, can be as large as 15,000 kilometers following a cold start.

Two sets of satellite ephemeris and timing accuracy are also used between the four scenarios. In the first set of cases, the batch filter is assumed to have full knowledge of the satellite ephemerides and transmitter clock frequency offset. The second set of cases introduces some errors into the satellite position, velocity, and clock offset rate. The receivers per-axis knowledge of each satellite's position vector is assumed to have error sampled from a Gaussian distribution with a mean of 0 and a standard deviation of 2 meters. The receivers per-axis knowledge of each satellites velocity vector is assumed to have error sampled from a Gaussian distribution with a mean of 0 and a standard deviation of 0.002 m/sec. The receivers knowledge of each satellites clock frequency offsets are assumed to have error sampled from a zero-mean Gaussian distribution with a standard deviation of 3.3×10^{-11} seconds/second. Along with satellites utilizing some sort of high quality oscillator, Psiaki proposes in [38] that this level of accuracy could be achieved with a ground segment to track and update the satellites' ephemeris.

3.4 GDOP Calculations

The Geometric Dilution of Precision derivation for the traditional psuedorange-based navigation equations is presented in Section 2.4. With this new proposed carrier Doppler shift navigation method, an alternative GDOP calculation is also necessary. As Psiaki states in [38], the carrier Doppler shift calculation in Equations 3.23 and 3.6 is too complicated for a GDOP analysis. Instead, a simplified analytical carrier

Doppler shift model is proposed in [38]:

$$-\lambda D^j = \frac{(\hat{\rho}^j)^\top(\vec{v}-\vec{v}^j)\left\{\frac{1+\frac{d\delta^j}{dT^j}}{1+\frac{1}{c}[a^j_{\delta tp}-(\hat{\rho}^j)^\top\vec{v}^j]}\right\}+c\frac{d\delta_R}{dT_R}-c\frac{d\delta^j}{dT^j}}{1+\frac{d\delta_R}{dT_R}} \tag{3.24}$$

where $\frac{d\delta_R}{dT_R}$ is the unknown receiver clock offset rate, $\frac{d\delta^j}{dT^j}$ is the satellite clock offset rate, T^j is the time of signal transmission, and $a^j_{\delta tp}$ is a term that arises from the time rate of change of the propagation delay of the signal. Some assumptions can be made to further simplify Equation 3.24. The effects due to the ionosphere and troposphere have already been omitted. The following approximations can also be made:

$$1 \approx 1+\frac{d\delta_R}{dT_R}$$

$$1 \approx 1+\frac{d\delta^j}{dT^j}$$

$$1 \approx 1+\frac{1}{c}[a^j_{\delta tp}-(\hat{\rho}^j)^\top\vec{v}^j]$$

Due to the likely stability of the receiver and satellite oscillators, the first two approximations can be made and due to the speed of the satellites relative to the speed of light, the third approximation can be made. Following the approximations, Equation 3.24 is simplified to:

$$-\lambda D^j = (\hat{\rho}^j)^\top(\vec{v}-\vec{v}^j)+c\frac{d\delta_R}{dT_R}-c\frac{d\delta^j}{dT^j} \tag{3.25}$$

Similar to a pseudorange-based GDOP analysis, a linearized relationship must be developed between the errors in the Doppler measurements and the errors in the filter's estimated quantities. Using the Doppler shift approximation in Equation 3.25,

the linearized relationship is

$$\begin{bmatrix} -\lambda\Delta D^1 \\ -\lambda\Delta D^2 \\ -\lambda\Delta D^3 \\ \vdots \\ -\lambda\Delta D^N \end{bmatrix} = \begin{bmatrix} (\hat{\dot{\rho}}^1)^\top & [(\hat{\rho}^1)^\top \dot{\vec{v}}^1 + (\hat{\dot{\rho}}^1)^\top \vec{v}^1] & (\hat{\rho}^1)^\top & c \\ (\hat{\dot{\rho}}^2)^\top & [(\hat{\rho}^2)^\top \dot{\vec{v}}^2 + (\hat{\dot{\rho}}^2)^\top \vec{v}^2] & (\hat{\rho}^2)^\top & c \\ (\hat{\dot{\rho}}^3)^\top & [(\hat{\rho}^3)^\top \dot{\vec{v}}^3 + (\hat{\dot{\rho}}^3)^\top \vec{v}^3] & (\hat{\rho}^3)^\top & c \\ \vdots & \vdots & \vdots & \vdots \\ (\hat{\dot{\rho}}^N)^\top & [(\hat{\rho}^N)^\top \dot{\vec{v}}^N + (\hat{\dot{\rho}}^N)^\top \vec{v}^N] & (\hat{\rho}^N)^\top & c \end{bmatrix} \begin{bmatrix} \Delta\vec{r} \\ \Delta\delta_R \\ \Delta\vec{v} \\ \Delta\dot{\delta}_R \end{bmatrix} \tag{3.26}$$

where $\Delta\vec{r}$ is the error in the receiver's estimated ECEF position, $\Delta\delta_R$ is the error in the receiver's estimated clock offset, $\Delta\vec{v}$ is the error in the receiver's estimated ECEF velocity, and $\Delta\dot{\delta}_R$ is the error in the receiver's estimated clock offset rate.

Several issues arise from the initial derivation of Equation 3.26, being that for a GDOP analysis the N x 8 coefficient matrix must be non-dimensional and the elements of the 8 x 1 estimation error matrix must have the same units. The 8 x 1 estimation error matrix must also have the same units as the measurement errors, $\lambda\Delta D^j$, which is m/sec. Looking at the N x 8 coefficient matrix, the first 3 columns have units of 1/seconds, the 4th column has units of m/sec^2, columns 5 through 7 are non-dimensional, and column 8 has units of m/sec. Looking at the 8 x 1 error estimation matrix, the units of $\Delta\vec{r}$ are meters, the units of $\Delta\delta_R$ are seconds, the units of $\Delta\vec{v}$ are m/sec, and $\Delta\dot{\delta}_R$ is non-dimensional. With units of m/sec already, the velocity error estimation term can be left in its current state. The clock offset rate error estimation term can simply be multiplied by the speed of light, which changes the units to m/sec. The re-scaling factors for $\Delta\vec{r}$ and $\Delta\delta_R$ are more complicated. In [38], Psiaki derives the scaling factors to be applied to the position and clock offset error estimation terms:

$$\gamma = \left(\frac{1}{1-(R_E/a_{orb})}\right)\sqrt{\frac{\mu}{a_{orb}^3}}$$

$$\eta = \left(\frac{(R_E/a_{orb})}{1-(R_E/a_{orb})}\right)\sqrt{\frac{\mu}{a_{orb}^2}},$$

where R_E is the radius of the Earth, a_{orb} is the semi-major axis of the satellite's

orbit, and μ is the standard gravitational parameter. γ has units of 1/sec and can be multiplied by $\Delta\vec{r}$ to give units of m/sec. η has units of m/sec^2 and can be multiplied by $\Delta\delta_R$ to also give units of m/sec. With all of the re-scaling factors applied, Equation 3.26 can be rewritten as

$$\begin{bmatrix} -\lambda\Delta D^1 \\ -\lambda\Delta D^2 \\ -\lambda\Delta D^3 \\ \vdots \\ -\lambda\Delta D^N \end{bmatrix} = \mathbf{A}_{GDOP} \begin{bmatrix} \gamma\Delta\vec{r} \\ \eta\Delta\delta_R \\ \Delta\vec{v} \\ c\Delta\dot{\delta}_R \end{bmatrix}$$

where

$$\mathbf{A}_{GDOP} = \begin{bmatrix} (\hat{\dot{\rho}}^1)^\top/\gamma & [(\hat{\rho}^1)^\top\dot{\vec{v}}^1 + (\hat{\dot{\rho}}^1)^\top\vec{v}^1]/\eta & (\hat{\rho}^1)^\top & 1 \\ (\hat{\dot{\rho}}^2)^\top/\gamma & [(\hat{\rho}^2)^\top\dot{\vec{v}}^2 + (\hat{\dot{\rho}}^2)^\top\vec{v}^2]/\eta & (\hat{\rho}^2)^\top & 1 \\ (\hat{\dot{\rho}}^3)^\top/\gamma & [(\hat{\rho}^3)^\top\dot{\vec{v}}^3 + (\hat{\dot{\rho}}^3)^\top\vec{v}^3]/\eta & (\hat{\rho}^3)^\top & 1 \\ \vdots & \vdots & \vdots & \vdots \\ (\hat{\dot{\rho}}^N)^\top/\gamma & [(\hat{\rho}^N)^\top\dot{\vec{v}}^N + (\hat{\dot{\rho}}^N)^\top\vec{v}^N]/\eta & (\hat{\rho}^N)^\top & 1 \end{bmatrix}.$$

Looking back to Section 2.4, the final 4 columns of $\mathbf{A}_{GDOP}$ represent the corresponding matrix in the GDOP analysis for a traditional pseudorange-based solution. As with the pseudorange-based solution, the scalar GDOP value can be derived using $\mathbf{A}_{GDOP}$.

$$GDOP = \sqrt{tr[(\mathbf{A}_{GDOP}^\top\mathbf{A}_{GDOP})^{-1}]} \tag{3.27}$$

3.5 Summary

Chapter 3 introduced the LEO constellations that are under investigation in this research. Four large LEO constellations, as well as two multi-constellation solutions, are tested in the navigation simulation. The mathematics behind the proposed carrier Doppler shift navigation method are also presented. An introduction to the simulation, along with the necessary initial conditions, was provided. Four different sets of initial conditions are used in this simulation, with their differences being in initial receiver state errors and the assumed errors in satellite ephemeris and timing data.

Each of the four scenarios were run a total of 100 times. Finally, equations to perform a GDOP analysis are derived. Chapter 4 contains the results of the GDOP analysis as well as the results of the simulation, each when using the different constellations described above.

4. Results

This chapter presents the results from this research, along with observations and analysis. Section 4.1 provides the results from the GDOP analysis for each of the constellations of interest. Section 4.2 presents PVT performance results from each of the simulation scenarios.

4.1 GDOP Results

GDOP analysis, using the equations from Section 3.4, was conducted for each of the constellations described in Section 3.1. The constellation designs in Tables 3.1-3.6 were used for this analysis. For each constellation, a three dimensional plot of GDOP versus latitude and longitude has been generated. In order to provide a better visual of the GDOP values, an additional GDOP versus latitude plot has been provided for some of the constellations. The latitude versus GDOP plots were generated by taking an average of GDOP at each latitude, which results in some of the asymmetries above/below the equator. Please note that the GDOP values were capped at 25 to ensure that any extremely high GDOP values did not distort the figures.

The GDOP statistics for the Kuiper constellation are shown in Figure 4.1. As discussed in Chapter 3, the small signal footprint of LEO satellites necessitates a constellation with near polar orbit vehicles in order to provide coverage at the poles. The Kuiper constellation will operate with satellite inclinations of 33.0, 42.0, and 51.9 degrees. Figure 4.2 shows that the lack of satellites at higher inclinations results in zero coverage above approximately ± 60 degrees. However, the large number of satellites at mid-inclinations provide moderate GDOP at $\pm 60 - \pm 50$ degrees and good user-satellite geometry below ± 50 degrees. The projected Kuiper constellation is a good example of a constellation that could benefit from utilizing another constellation

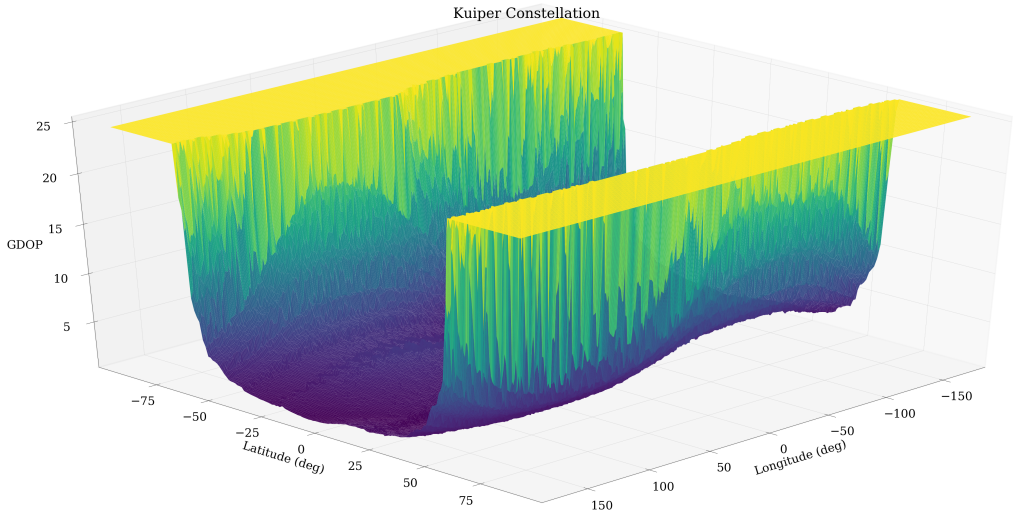

Figure 4.1. GDOP vs. Latitude/Longitude for Kuiper Constellation

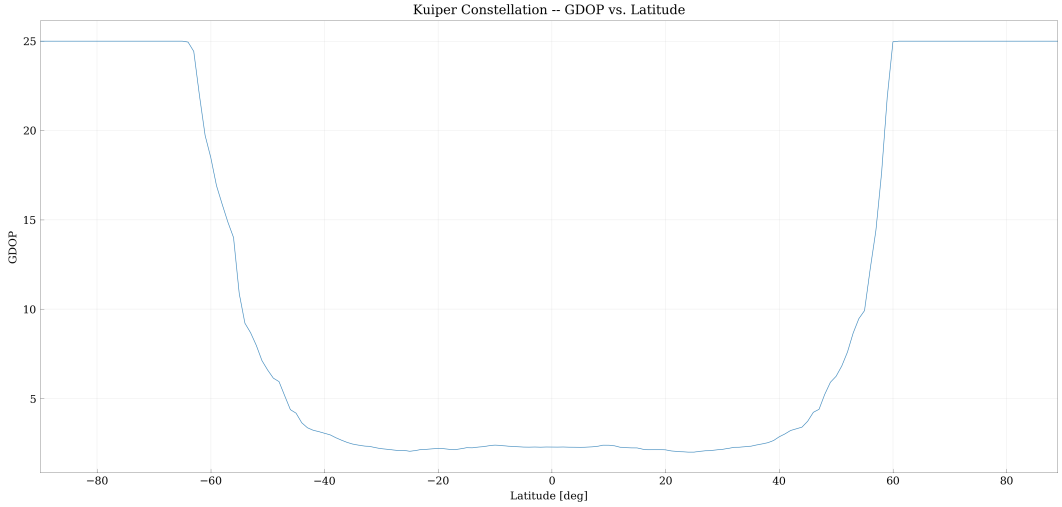

Figure 4.2. GDOP vs. Latitude for Kuiper Constellation

that operates satellites in near polar orbit. Even a smaller constellation, such as Iridium NEXT or Telesat, could provide the coverage necessary to make the Kuiper constellation a viable option for this navigation method.

The GDOP statistics for the OneWeb constellation are shown in Figure 4.3. Unlike Kuiper, the OneWeb constellation provides sufficient coverage at the poles, with inclinations of 40.0, 55.0, and 87.9 degrees. The large number of satellites at each inclination results in the largest GDOP value being below 0.9, which is excellent. It can be observed that the GDOP across the majority of the Earth is below 0.5, with two lobes that peak at approximately 0.9 at the equator and longitudes of $\pm$ 100 degrees. This increase in GDOP is most likely the result of most satellites traveling in the same direction (north or south) at those particular regions. While the peak in GDOP still results in excellent geometry, it illustrates the fact that GDOP is more than just a function of number of satellites and their inclinations.

The GDOP statistics for the Starlink constellation are shown in Figure 4.4. With the Starlink constellation, the same behavior is observed from the Kuiper constellation, only less severe. GDOP values for Starlink reach highs of around 10 near the poles, which still allows for moderate user-satellite geometry. Looking at the constellation design, Starlink plans call for 11,914 satellites at inclinations of 42.0, 48.0, 53.0, 53.2, 70, and 97.6 degrees. Note that the Starlink plans do call for near polar satellites, but the number is much smaller in comparison to mid-inclination satellites. This, along with direction of satellite travel, is a contributor to the regions of increased GDOP. Figure 4.5 provides a look at GDOP versus latitude. The figure has the same ramp shape of Kuiper's Figure 4.2, where the mid latitude regions between -60 and +60 degrees have excellent GDOP. The difference being that the Starlink constellation is still able to provide good geometry to the areas above +60 degrees and below -60 degrees latitude. Starlink is by far the largest proposed LEO

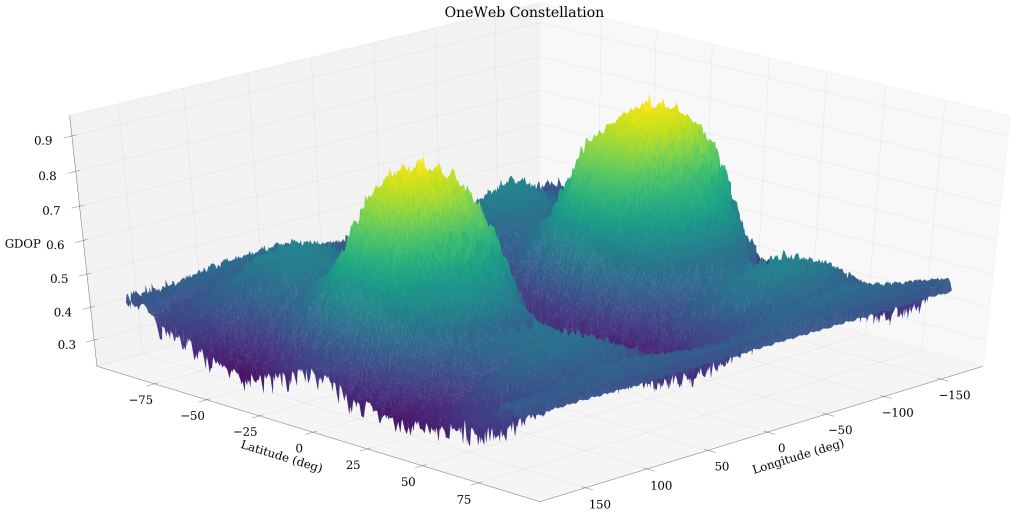

Figure 4.3. GDOP vs. Latitude/Longitude for OneWeb Constellation

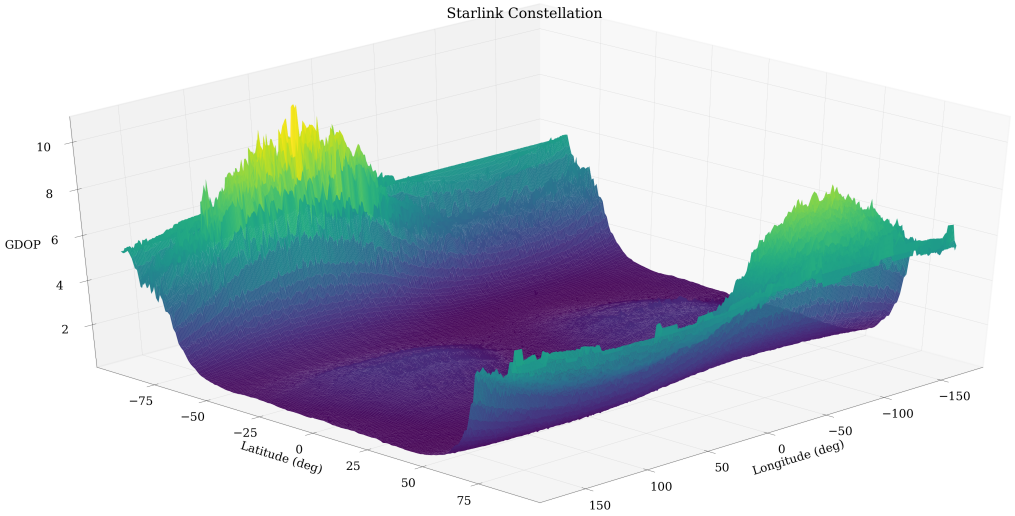

Figure 4.4. GDOP vs. Latitude/Longitude for Starlink Constellation

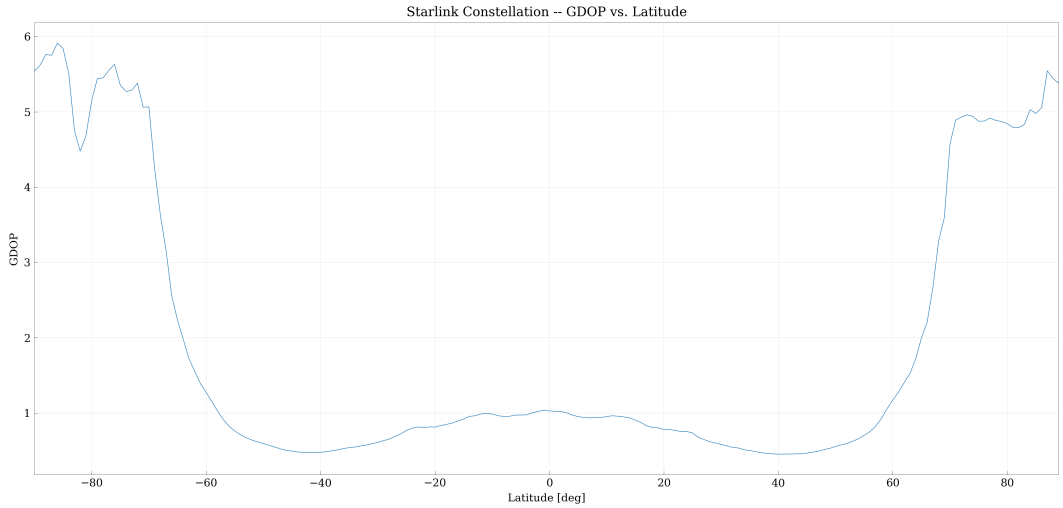

Figure 4.5. GDOP vs. Latitude for Starlink Constellation

constellation, but again, sheer number of satellites is not the sole driving factor of user-satellite geometry. As with the Kuiper constellation, this version of the Starlink constellation could leverage another small LEO constellation to improve geometry at and around the poles.

The GDOP statistics for the Telesat constellation are shown in Figure 4.6. Out of the constellations individually considered in this research, Telesat is the smallest. With only 298 satellites projected at inclinations of 45.0 and 88.0 degrees, Figure 4.6 shows a large number of coverage gaps over the surface of the Earth. Even though the constellation does have plans for high-inclination satellites, the relatively small number still result in poor coverage at the poles. It's noteworthy that there appears to be much less symmetry across latitude and longitude for the Telesat GDOP values compared to the other constellations. Figure 4.7 illustrates this for the latitude values. Again, the lack of symmetry could be due in part to the averaging of GDOP along longitude, but the lower number of satellites also plays a role. Unlike traditional pseudorange-based navigation, there is a need for 8 visible satellites to generate PVT.

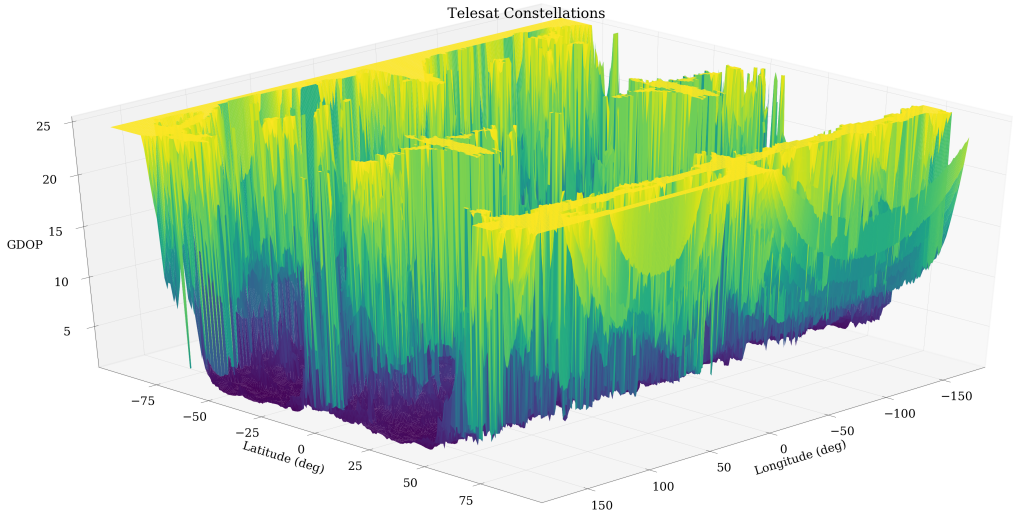

Figure 4.6. GDOP vs. Latitude/Longitude for Telesat Constellation

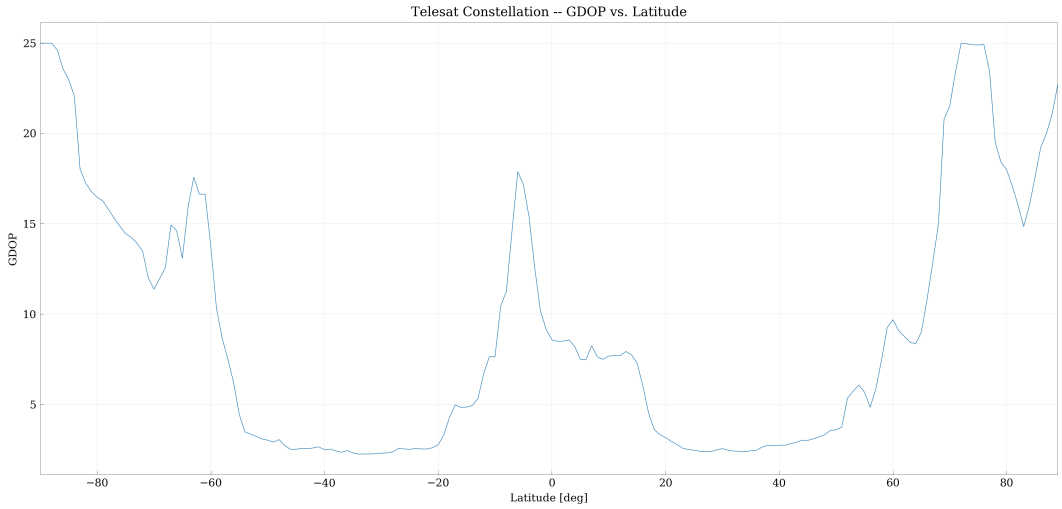

Figure 4.7. GDOP vs. Latitude for Telesat Constellation

As Figures 4.6 and 4.7 illustrate, the Telesat constellation can provide sufficient coverage for patches of the Earth, but additional satellites or better constellation design are necessary for total global coverage. Somewhat dependent on longitude, the Telesat constellation results in moderate to good GDOP values between approximately ± 70 and ± 5 degrees latitude.

The GDOP statistics for the current multi-constellation solution are shown in Figure 4.8. The current multi-constellation solution contains satellites from the Iridium NEXT, OneWeb, and Starlink constellations at inclinations of 53.0, 86.4, 87.9, and 97.6 degrees. Similar to the Telesat constellation, the GDOP values from the current multi-constellation solution are more erratic than the other constellations. This is due to the fact that 2 out of the 3 constellations utilized are not fully operational. Iridium NEXT is the only fully operational constellation, while the other 2 have only begun to launch vehicles. The constellation that results from satellites in orbit as of April 8th, 2021 is much less symmetrical than it would be once fully operational. With that said, outside of a few spikes at and around the equator, the current constellation provides good user-satellite geometry across the Earth. Iridium NEXT, OneWeb, and Starlink all provide satellites at high-inclinations to cover the poles. Starlink also provides a large number of vehicles at mid-inclination which covers the rest of the Earth. As discussed, the areas where GDOP increases is largely due to the incomplete OneWeb and Starlink constellations.

The GDOP statistics for the future multi-constellation solution are shown in Figure 4.9. Table 3.6 lists all of the different inclinations that the combination of constellations operate at, which range from 33.0 to 87.9 degrees. The largest GDOP value from Figure 4.9 is below 0.7 which means the entire Earth has excellent user-satellite geometry. Looking at the shape of the plot, it looks familiar to the Kuiper and Starlink plots, where GDOP is very good below -60 and above +60 degrees but increases

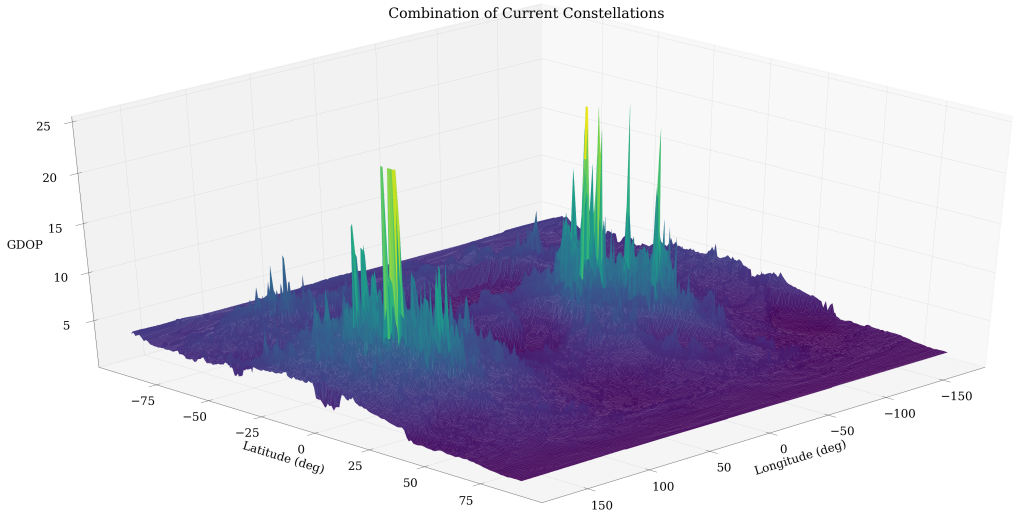

Figure 4.8. GDOP vs. Latitude/Longitude for Iridium, OneWeb, and Starlink Constellations as of April 8th, 2021

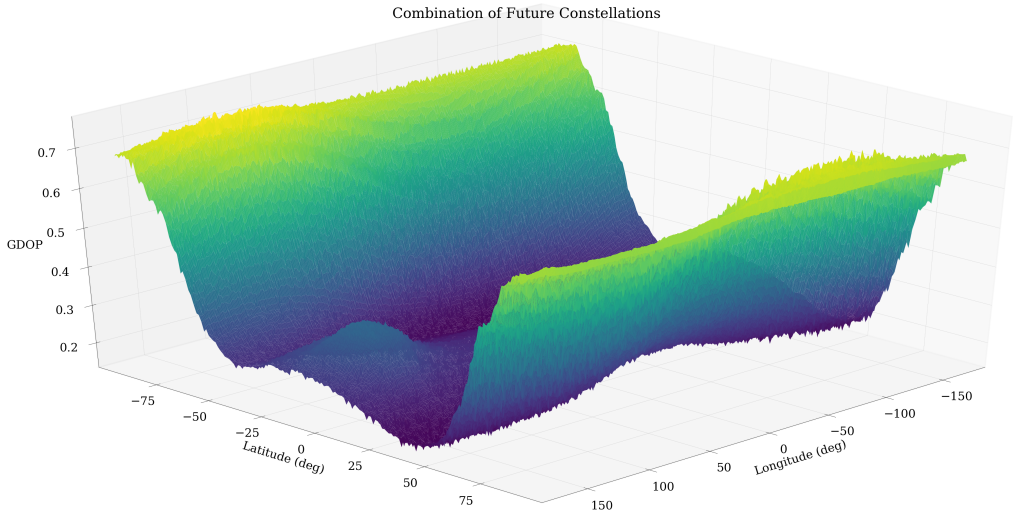

Figure 4.9. GDOP vs. Latitude/Longitude for Future Kuiper, OneWeb, Starlink, and Telesat Constellations

closer to the poles. The plot shape along the equator also takes the same shape as the OneWeb plot with 2 noticeable peaks and otherwise excellent GDOP. Being that Kuiper, OneWeb, and Starlink make up the majority of this multi-constellation solution, it should come as no surprise that the GDOP plot bears a resemblance.

4.2 Simulated PVT Performance Results

The simulated PVT results when using each of the discussed constellations are shown below. A table of statistics is presented for each of the constellations to express the performance. There are 10 columns in each table. The first column is labeled 'Scenario' and denotes which of the four simulation scenarios the data corresponds to. The simulation scenarios can be found in Table 3.7. The second column is labeled 'Unconverged' and communicates the number of cases, out of 100, that did not converge. In this case, the term unconverged means that the filter on a particular simulation either converged on an incorrect solution, or reached the maximum number of Gauss-Newton iterations without converging. The maximum number of iterations was set to 30 for every simulation. The third and fourth columns denote the maximum number of iterations and the mean number of iterations out of the converged cases, respectively. The next six columns are the maximum final error and RMS error of the receiver position, velocity, and clock offset when compared to the truth values. It is important to note that the maximum and RMS clock offset error values in columns 9 and 10 are in units of milliseconds. The clock offset rate errors will be discussed later in this chapter.

From the perspective of a receiver's ability to generate accurate PVT, the simulation scenarios proceed in order from easiest to hardest. Scenario 1a can be considered the easiest because the initial error is bounded and the satellite ephemerides and timing are assumed to be error free. On the other hand, Scenario 2b begins from a cold

start and there exists some assumed error in the satellite PVT. In general, each of the constellation statistics reflect this. Additional observations are provided below, including a comparison of the simulation performance between each constellation.

Table 4.1 contains the statistics from each of the four simulation scenarios with the Kuiper constellation. Beginning with column 2, Scenario 1a had the fewest number of unconverged cases with 24, while Scenario 2b had 75 such cases. This falls in line with the idea that Scenario 1a should be the easiest and Scenario 2b should be the hardest. The GDOP values presented in Figure 4.1 illustrate the poor coverage at and around the poles. For Scenarios 1a and 1b, the cases where the filter did not converge more than likely stem from a truth location with a lack of coverage. The same can partially be said for Scenarios 2a and 2b, but the challenging initial conditions play a large part in why upwards of 70% of the cases did not converge. The maximum and mean iterations are similar for Scenarios 1a and 1b and Scenarios 2a and 2b. When the initial error is bounded, the filter was able to converge in an average of 3 iterations. The number of mean iterations jumped to approximately 8 for Scenarios 2a and 2b. Error in the initial receiver state had an obvious impact on both the filter's ability to converge and the time it took to converge. Turning to the filter's convergence accuracy, a pattern also exists between results from Scenarios 1a and 2a and Scenarios 1b and 2b. The difference between these sets of Scenarios is the assumed error in the satellite ephemerides and timing. The pattern is especially noticeable in the position error statistics where the RMS position error jumps from below 1 meter up to several meters from Scenarios 1a and 2a to Scenarios 1b and 2b. The pattern is present but less pronounced in the velocity error results. When compared to expected receiver errors using GPS and traditional pseudorange-based navigation, both the position and velocity errors are on par. The clock offset errors are significantly worse and as Psiaki points out in [38], the reason for this larger clock

Table 4.1. Simulation Results - Kuiper Constellation

Scenario	Unconverged	Max Iterations	Mean Iterations	Max Pos. Error $[m]$	RMS Pos. Error $[m]$	Max Vel. Error $[\frac{m}{s}]$	RMS Vel. Error $[\frac{m}{s}]$	Max Clk. Off. Error $[ms]$	RMS Clk. Off. Error $[ms]$
1a	24	4	3.05	1.6701	0.403	0.0067	0.0016	0.1156	0.0301
1b	29	4	3.04	4.3776	3.1082	0.0097	0.0022	0.1294	0.0287
2a	71	14	8.14	0.9052	0.1785	0.0043	0.0011	0.1581	0.0313
2b	75	11	7.76	3.3722	2.5556	0.0047	0.0017	0.0869	0.0294

Table 4.2. Simulation Results - OneWeb Constellation

Scenario	Unconverged	Max Iterations	Mean Iterations	Max Pos. Error $[m]$	RMS Pos. Error $[m]$	Max Vel. Error $[\frac{m}{s}]$	RMS Vel. Error $[\frac{m}{s}]$	Max Clk. Off. Error $[ms]$	RMS Clk. Off. Error $[ms]$
1a	0	3	2.99	1.9858	0.1986	0.0094	0.0009	0.5011	0.0501
1b	0	3	2.99	2.3576	2.2494	0.0245	0.0024	1.5913	0.1591
2a	53	11	6.4	2.132	0.3729	0.0247	0.0036	3.005	0.4394
2b	58	10	6	3.9417	3.5552	0.0066	0.0014	0.7415	0.1427

Table 4.3. Simulation Results - Starlink Constellation

Scenario	Unconverged	Max Iterations	Mean Iterations	Max Pos. Error $[m]$	RMS Pos. Error $[m]$	Max Vel. Error $[\frac{m}{s}]$	RMS Vel. Error $[\frac{m}{s}]$	Max Clk. Off. Error $[ms]$	RMS Clk. Off. Error $[ms]$
1a	0	3	3	1.7747	0.3254	0.019	0.0027	0.2587	0.0415
1b	0	4	3.01	5.8615	4.8332	0.0199	0.0028	0.1944	0.0402
2a	37	11	6.4	1.9447	0.3957	0.0072	0.0015	0.1677	0.0382
2b	48	15	6.6	5.9717	4.8417	0.377	0.0056	1.4651	0.197

offset error stems from the maximum value of the acceleration of the satellite relative to the receiver. This acceleration is not large enough to replicate the timing accuracy from pseudorange-based navigation systems. This will be true for the clock offset error results from each constellation considered in this research.

Table 4.2 contains the statistics from each of the four simulation scenarios with the OneWeb constellation. The number of unconverged cases follows the same pattern of the Kuiper constellation. However in the bounded initial error scenarios, the OneWeb constellation did not have a single unconverged case. The lack of coverage gaps in the OneWeb GDOP plot contribute to the 100% convergence rate from these 2 simulation scenarios. The number of unconverged cases rises to 53 and 58 respectively for Scenario 2a and Scenario 2b. While there is improvement in comparison to the Kuiper constellation, the convergence rate still falls below 50%. Even with excellent user-satellite geometry over the entire Earth, the simulation still struggles to converge following a cold start. This points to the difficulty of a scenario where the receiver has no prior knowledge of its state. In line with results from the Kuiper constellation, the mean number of iterations roughly doubled from 3 to 6 when going from bounded initial errors to cold start. The receiver maximum and RMS position error follow the pattern of imperfect satellite observables leading to increased error values in Scenarios 1b and 2b. As with other constellations, the position and velocity errors compare favorably to GPS while the clock offset errors do not.

Table 4.3 contains the statistics from each of the four simulation scenarios with the Starlink constellation. As far as convergence rate, Starlink performs the best out of any of the individual constellations considered in this simulation. The bounded initial error scenarios resulted in 100% convergence rate while the cold start scenarios resulted in 63% and 52% convergence rate, respectively. Though the Starlink GDOP values reach peaks greater than OneWeb around the poles, the massive number of

satellites allows for a higher convergence rate. The increased GDOP manifests in the receiver state errors where larger errors are observed when compared to the OneWeb results. Again, the satellite errors lead to an increase in the maximum and RMS receiver state errors. Position and velocity errors also fall in line with those from GPS-based navigation while clock offset errors do not. It's interesting that convergence rate appears to be more of a function of pure satellite number and coverage where receiver errors rely more on the user-satellite geometry.

Table 4.4 contains the statistics from each of the four simulation scenarios with the Telesat constellation. The convergence rate increased with the scenario number which is consistent with the other constellations. Interestingly, the Telesat constellation convergence rates are slightly better than the Kuiper constellation. With only 298 satellites, the Telesat constellation is roughly 1/10th the size of Kuiper and while it is not without geometry issues, the polar orbit satellites help mitigate total coverage lapses. Looking at Figures 4.2 and 4.7 might seem hard to believe the convergence rates of Telesat are better than Kuiper. However, a much larger portion of the Kuiper plot reports lack of coverage (GDOP > 25). The GDOP values are moderate at best for the Telesat plot, but there are smaller areas of insufficient coverage. The maximum number of iterations in column 3 suggest that the filter struggled to converge more so than other constellations. The errors in columns 5-10 reflect this as well. The maximum and RMS values are the largest of any constellation. Similar to the Starlink constellation, the better overall Earth coverage with sometimes degraded GDOP values result in higher convergence rates and larger receiver state errors. Even with the larger receiver errors, they are still comparable to values from the other tables.

Table 4.5 contains the statistics from each of the four simulation scenarios with the current multi-constellation solution. With satellites from the Iridum NEXT, OneWeb, and Starlink constellations, this constellation resulted in 100% convergence in Sce-

Table 4.4. Simulation Results - Telesat Constellation

Scenario	Unconverged	Max Iterations	Mean Iterations	Max Pos. Error $[m]$	RMS Pos. Error $[m]$	Max Vel. Error $[\frac{m}{s}]$	RMS Vel. Error $[\frac{m}{s}]$	Max Clk. Off. Error $[ms]$	RMS Clk. Off. Error $[ms]$
1a	18	13	3.3	2.18	0.39	0.0544	0.0072	0.3614	0.0654
1b	22	10	3.27	4.2986	4.0543	0.0081	0.0012	0.3008	0.0322
2a	58	14	7.51	1.898	0.5312	0.0103	0.0025	0.3329	0.0692
2b	65	18	7.49	7.3525	6.0159	0.0222	0.0036	0.4037	0.0702

Table 4.5. Simulation Results - Current Constellation of Constellations

Scenario	Unconverged	Max Iterations	Mean Iterations	Max Pos. Error $[m]$	RMS Pos. Error $[m]$	Max Vel. Error $[\frac{m}{s}]$	RMS Vel. Error $[\frac{m}{s}]$	Max Clk. Off. Error $[ms]$	RMS Clk. Off. Error $[ms]$
1a	0	4	3.14	1.6424	0.3324	0.0109	0.0016	0.0941	0.0216
1b	0	4	3.04	5.2549	3.9802	0.0149	0.0022	0.4236	0.0668
2a	42	24	8.06	1.4636	0.4094	0.0104	0.0028	0.2606	0.0561
2b	48	22	8.52	5.6644	4.2519	0.0103	0.0021	0.4544	0.0859

Table 4.6. Simulation Results - Future Constellation of Constellations

Scenario	Unconverged	Max Iterations	Mean Iterations	Max Pos. Error $[m]$	RMS Pos. Error $[m]$	Max Vel. Error $[\frac{m}{s}]$	RMS Vel. Error $[\frac{m}{s}]$	Max Clk. Off. Error $[ms]$	RMS Clk. Off. Error $[ms]$
1a	0	3	3	0.1603	0.0361	0.0002	0.00005	0.0144	0.0037
1b	0	4	3.14	1.6424	0.3324	0.0109	0.0016	0.0941	0.0216
2a	15	10	6.71	1.5552	0.4275	0.0093	0.0018	0.4807	0.1058
2b	24	14	6.67	3.9477	2.6788	0.0099	0.0016	1.1258	0.138

narios 1a and 1b and 58% and 52% convergence in Scenarios 2a and 2b, respectively. With less than half the satellites of Kuiper, this constellation outperformed it due to the diversity of its satellite coverage. Another constellation struggling to reach 60% convergence during the cold start scenarios points to the difficulty of this condition for the proposed navigation method. The maximum number of iterations for Scenarios 2a and 2b also support this idea. Initializing at position errors up to 15,000 kilometers leads to a large number of Gauss-Newton iterations to reach convergence. Consistent with other simulation results, the satellite ephemeris and timing errors lead to increased receiver state errors, most obvious for the position vector. The position and velocity errors are also comparable to expected error from pseudorange-based GPS navigation.

Table 4.6 contains the statistics from each of the four simulation scenarios with the future multi-constellation solution. The final simulations were run using a constellation combining the proposed fully operational constellations of Kuiper, OneWeb, Starlink, and Telesat. Similar to several of the constellations already discussed, the constellation of over 20,000 satellites produced a 100% convergence rate for Scenarios 1a and 1b. The mega-constellation also provided by far the best convergence rate in the cold start scenarios, with rates of 85% and 76%. Improvements in the convergence rate are attributed to the size of the constellation. The maximum and mean iterations are similar to those from OneWeb and Starlink, the other two constellations with a large number of satellites and good global GDOP. Assumed errors in the satellite ephemerides and timing once again lead to larger final errors in the receiver states. Almost all of the errors in Table 4.6 represent the smallest such values in any of the simulation result tables. The number of satellites, number of planes, number of inclinations, and overall GDOP results contribute to this constellation providing the best performance.

The tables and observations above lead to several conclusions. The first being that the convergence rates from Scenarios 1a and 1b are more closely tied to the constellation size and design than Scenarios 2a and 2b. The apparent difficulty of a cold start condition on the navigation method presented lead to mediocre convergence rates. Another conclusion that can be drawn is that convergence rate is more dependent on satellite coverage (8 or more) while receiver errors are more a function of user-satellite geometry. The Kuiper and Telesat comparison illustrates this. While Telesat provides higher convergence rates, the converged cases tend to have larger errors than those of Kuiper. An observation that has been touched on several times is the effect of satellite timing and ephemeris errors on the final receiver errors.

The maximum and RMS receiver clock offset rate errors were not presented for any of the simulations. The error values from each simulation are on the order of 1×10^{-12} or better which when multiplied by the speed of light, $c\dot{\delta}_R$, result in errors better than 0.001 m/sec. This is similar to the velocity estimates and represents a negligible error from the receiver's perspective. The clock offset rate errors are comparable to a GPS navigation system.

4.3 Summary

The GDOP and simulation results from each of the considered constellations were presented in this chapter. Through analysis of both results, the suitability of each constellation to potentially provide navigation services can be determined. It should be stated that none of the constellations are currently designed with navigation services in mind. Combining observations from the GDOP and simulation results, Kuiper and Telesat can be deemed the least suitable to support navigation in their currently planned state. The remaining 4 each have their pros and cons, but all show promise in being able to successfully be utilized for navigation. The cold start scenarios did

present convergence issues for each constellation, but having zero prior knowledge of the receiver state is a somewhat less likely scenario. Regardless, there is at least some demonstrated feasibility of each constellation allowing a receiver to navigate using its observed carrier Doppler shift.

5. Conclusion and Recommendations

5.1 Results

In [38], a novel navigation method using simultaneous carrier Doppler shift measurements from 8 LEO satellites was introduced. The algorithm solved for receiver position, clock offset, velocity, and clock offset rate. Simulations were conducted in order to test the feasibility of this method using the then-projected 2,825 satellite Starlink constellation. With advancements made in both the number and size of projected LEO constellations, the goal of this thesis was to extend the research presented in [38]. This thesis research considered 4 separate large LEO constellations, as well as 2 multi-constellation solutions. Another goal of the work was expanding the initial receiver conditions in an attempt to explore the batch filter's ability to converge following a cold start.

Through the use of both NORAD-maintained and fabricated TLE files and an orbit propagator, a Python simulation was created to facilitate this exploration. With the equations derived in Chapter 3, a GDOP analysis was also performed to help project the user-satellite geometry achievable. The results in Chapter 4 help to answer some of the questions this research set out to address. Firstly, the GDOP plots in Chapter 4 illustrate that all 6 constellations investigated provide good user-satellite geometry over portions of the Earth. The larger constellations do this better than the smaller ones, but the results suggest navigating this way is feasible. It should also be pointed out again that these results are from constellations whose designs have not been optimized for this application.

Scenarios 1a and 1b, which are cases where the initial receiver errors are bounded, were derived directly from [38] and were included to validate the credibility of the simulation. Outside of the constellations with few satellites (Telesat) and known

coverage gaps (Kuiper), all simulations performed in line with those presented in [38]. Given this, the results of the other 2 scenarios can be presented with some confidence. Scenarios 2a and 2b, which are cases with unbounded initial receiver errors, were used to simulate a receiver that has just been cold started and has no knowledge of its position, clock offset, velocity, and clock offset rate. The cold start scenarios had a clear effect on the filter's ability to converge on an accurate solution. None of the constellations had a convergence rate higher than 85%, which the future multi-constellation solution achieved during the 100 cases of Scenario 2a. This is not ideal as a standalone navigation system should not be handicapped in the case of a cold start. Additional work could be done to explore methods to help move this convergence rate closer 100% following a cold start. However, even the convergence rates shown in this research are promising.

5.2 Significance of Study

As mentioned, the main goal of this research was to expand upon the work presented in [38]. In the process of replicating the work, several useful Python scripts were generated that can be leveraged for future work. Given a constellation design – number of satellites, planes, and inclinations – the TLE fabrication script can generate the necessary TLE files for use in the actual simulation. When used in conjunction with the GDOP analysis script, a quick glimpse at the global user-satellite geometry can be generated. The actual simulation script was designed to be user-friendly where constellation(s) of choice, initial conditions, and other simulation parameters can easily be modified.

Another contribution of this research is the exploration of new large LEO constellations. Even since the original paper was published, there have been updates to the planned constellations for several technology companies. Plans for new constel-

lations mean that LEO traffic could reach numbers of 50,000 in the next 10 years and there is a clear opportunity to leverage them for navigation. While the use of GPS will continue to be extensive, the ever-evolving threats to it necessitate robust backups. Large LEO constellations should be one of the leading research candidates. This research successfully attempted to explore additional LEO constellations, including multi-constellation solutions, using the proposed carrier Doppler shift navigation method. The original work was also expanded to include the simulation results following a cold start of a receiver. The performance of these novel constellations was presented in the form of GDOP plots and simulation result comparison.

5.3 Limitations of Study

A number of assumptions are made in this research that would potentially need to be addressed in future work. The first assumption has to do with a receiver's ability to track the LEO signals. This simulation assumes that any satellite appearing to the user above a 7.5 degree elevation mask provides a usable Doppler shift measurement. The first reason this is unlikely is due to inevitable signal obstruction. Whether it is tree cover, urban canyon, or other natural obstructions, it is unlikely a receiver would be able to track every satellite above 7.5 degrees elevation. Another assumption made is that every satellite in view transmits a signal that reaches the user. GPS signals are transmitted such that a user will have simultaneous visibility of at least 4 satellites at all times. LEO constellations are currently designed for communication purposes and are not designed with simultaneous visibility in mind, therefore it might be unlikely to expect signal reception from every satellite in view. LEO constellations utilized for communication are designed to provide hand-off from one satellite to another above a certain elevation, in order to minimize the constellation size. Signal tracking and deconfliction is another problem not addressed in this research. Especially for the

multi-constellation solutions, the different LEO signals are transmitted at differing frequencies and modulation schemes. Multiple antenna's or an ultra-wideband antenna might be necessary to track signals from multiple constellations. In the event that LEO satellites do eventually provide simultaneous visibility, the massive number of satellites in some of these constellations would require signal deconfliction on the part of the receiver.

It is currently not clear if these LEO constellations intend to transmit any usable satellite ephemeris information, or what the level of accuracy would be available. The same goes for the level of timing accuracy available on LEO satellites. The size of GPS satellite vehicles allow them to carry multiple atomic clocks, but this is unrealistic for LEO satellites due to their size and cost. Work has been conducted to explore what type of ephemeris and timing accuracy would be necessary from LEO satellites in order to replicate the performance of GPS [39]. Fully leveraging these LEO constellations for navigation may require independent services that perform constellation monitoring to determine orbit and clock models. Until additional LEO constellations are leveraged for navigation, however, some assumptions must be made.

5.4 Future Work

Future work could be focused on exploring the assumptions made in this research. There has been significant work already completed in an attempt to blindly track LEO signals, which is an area that future work could be focused. Software defined radios can be utilized to track signals from one or multiple LEO constellations. An issue that has been covered in this research is the need for accurate satellite ephemeris and timing information. Chances are that LEO satellites, in their current state, are not equipped for such a task. Researching and prototyping a solution to this problem would be an excellent area of focus.

In addition, work should be focused on further improvements to the navigation simulation presented in this research. The less-than-ideal convergence rates observed during the cold start scenarios is one area that could benefit from additional research. There are likely auxiliary methods that can be implemented to improve the convergence following a receiver cold start. The constellation designs used in this research were taken directly from FCC filings. They have no doubt been optimized for the use they are intended for. Design and test of a navigation-optimized LEO constellation would be a good test case for the current simulation. There are also other test scenarios, outside of the 4 presented in this research, that would be good evaluations of a constellation's suitability for navigation services. Along with other current LEO research, the successful accomplishment of the goals set out for this research warrants further consideration of LEO constellations leveraged for navigation.

Bibliography

1. Control Segment. Accessed: 2021-10-26. [Online]. Available: https://www.gps.gov/systems/gps/control/

2. How GPS Receivers Work – Trilateration vs Triangulation. Accessed: 2021-10-25. [Online]. Available: https://gisgeography.com/trilateration-triangulation-gps/

3. Medium earth orbit. Accessed: 2022-01-26. [Online]. Available: https://en.wikipedia.org/wiki/Medium_Earth_orbit

4. NAVSTAR GPS. Accessed: 2021-10-25. [Online]. Available: https://www.e-education.psu.edu/geog862/node/1768

5. Oneweb satellite constellation. Accessed: 2022-01-26. [Online]. Available: https://en.wikipedia.org/wiki/OneWeb_satellite_constellation

6. Orbital elements. Accessed: 2022-01-27. [Online]. Available: https://en.wikipedia.org/wiki/Orbital_elements#Two-line_elements

7. Root mean square. Accessed: 2022-01-26. [Online]. Available: https://en.wikipedia.org/wiki/Root_mean_square

8. Starlink. Accessed: 2022-01-26. [Online]. Available: https://en.wikipedia.org/wiki/Starlink

9. Time to first fix. Accessed: 2022-01-27. [Online]. Available: https://en.wikipedia.org/wiki/Time_to_first_fix

10. Transit (satellite). Accessed: 2021-11-04. [Online]. Available: https://en.wikipedia.org/wiki/Transit_(satellite)

11. Two-line Element Set. Accessed: 2021-08-25. [Online]. Available: https://en.wikipedia.org/wiki/Two-line_element_set

12. C. T. Ardito, J. J. Morales, J. J. Khalife, A. A. Abdallah, and Z. M. Kassas, "Performance Evaluation of Navigation using LEO Satellite Signals with Periodically Transmitted Satellite Positions," *ION 2019 International Technical Meeting Proceedings*, pp. 306–318, 2019.

13. C. Bastos, R. Fernandes, R. Prata, J. M. Palomo Gutiérrez, A. Fernández, F. Darugna, M. Bardella, M. Sciarratta, S. Casotto, P. Giordano, and P. Zoccarato, "Triple-band GNSS Receiver with E6 HAS Corrections for Precise Onboard Orbit Determination in LEO," *Proceedings of the 34th International Technical Meeting of the Satellite Division of The Institute of Navigation (ION GNSS+ 2021)*, pp. 1053–1065, 2021.

14. C. Davenport. Thousands more satellites could soon be launched into space. Can the federal government keep up? The Washington Post. Accessed: 2022-01-27. [Online]. Available: https://www.washingtonpost.com/technology/2020/07/23/satellites-collisions-tracking-space/

15. Transit Satellite: Space-based Navigation. Defense Advanced Research Projects Agency. Accessed: 2021-11-04. [Online]. Available: https://www.darpa.mil/about-us/timeline/transit-satellite

16. F. Farhangian and R. J. Landry, "Multi-Constellation Software-Defined Receiver for Doppler Positioning with LEO Satellites," *Sensors (Switzerland)*, vol. 20, no. 20, pp. 1–17, 2020.

17. "FCC 94-268," Federal Communications Commission, pp. 189–191, 1994, Accessed: 2022-01-14. [Online]. Available: https://www.fcc.gov/document/orbital-communications-corporation-4

18. "DA 16-875," Federal Communications Commission, 2016, Accessed: 2022-01-14. [Online]. Available: https://docs.fcc.gov/public/attachments/DA-16-875A1.pdf

19. "FCC 18-161," Federal Communications Commission, pp. 40–42, 2018, Accessed: 2022-01-14. [Online]. Available: https://docs.fcc.gov/public/attachments/FCC-18-161A1.pdf

20. "Application to Modify Petition for Declaratory Ruling to Grant Access to the U.S. Market for Telesat's NGSO Constellation," Federal Communications Commission, 2020, Accessed: 2022-01-14. [Online]. Available: https://fcc.report/IBFS/SAT-MPL-20200526-00053/2378318.pdf

21. "FCC 20-102," Federal Communications Commission, pp. 8324–8347, 2020, Accessed: 2022-01-14. [Online]. Available: https://docs.fcc.gov/public/attachments/FCC-20-102A1.pdf

22. "Amendment to Modification Application for U.S. Market Access Grant for the OneWeb Ku- and Ka-Band System," Federal Communications Commission, 2021, Accessed: 2022-01-14. [Online]. Available: https://fcc.report/IBFS/SAT-MPL-20210112-00007/3495551.pdf

23. M. S. Floater, "Lecture 13 : Non-linear least squares and the Gauss-Newton method," 2018, Accessed: 2021-11-15. [Online]. Available: https://www.uio.no/studier/emner/matnat/math/MAT3110/h19/undervisningsmateriale/lecture13.pdf

24. P. E. Gill, W. Murray, and M. H. Wright, *Practical Optimization*. Academic Press, Inc., 1981.

25. G. Gutt, D. Lawrence, S. Cobb, and M. O'Connor, "Recent PNT Improvements and Test Results based on Low Earth Orbit Satellites," *Proceedings of the Annual Precise Time and Time Interval Systems and Applications Meeting, PTTI*, vol. 2018-Janua, pp. 72–79, 2018.

26. E. D. Kaplan and C. J. Hegarty, *Understanding GPS: Principles and Applications*, 2nd ed., 2006, p. 303.

27. Z. M. Kassas, M. Neinavaie, J. Khalife, N. Khairallah, J. A. Haidar-Ahmad, S. E. Kozhaya, and Z. Shadram, "ENTER LEO on the GNSS Stage: Navigation with Starlink Satellites," 2021. [Online]. Available: https://insidegnss.com/enter-leo-on-the-gnss-stage-navigation-with-starlink-satellites/

28. N. Khairallah and Z. M. Kassas, "Ephemeris Closed-Loop Tracking of LEO Satellites with Pseudorange and Doppler Measurements," *Proceedings of the 34th International Technical Meeting of the Satellite Division of The Institute of Navigation (ION GNSS+ 2021)*, no. March 2021, pp. 2544–2555, 2021.

29. J. Khalife and Z. M. Kassas, "Assessment of Differential Carrier Phase Measurements from ORBCOMM LEO Satellite Signals for Opportunistic Navigation," *Proceedings of the 32nd International Technical Meeting of the Satellite Division of the Institute of Navigation, ION GNSS+ 2019*, pp. 4053–4063, 2019.

30. J. J. Khalife and Z. M. Kassas, "Receiver Design for Doppler Positioning with LEO Satellites," *ICASSP, IEEE International Conference on Acoustics, Speech and Signal Processing - Proceedings*, vol. 2019-May, pp. 5506–5510, 2019.

31. S. E. Kozhaya, J. A. Haidar-Ahmad, A. A. Abdallah, Z. M. Kassas, and S. S. Saab, "Comparison of Neural Network Architectures for Simultaneous Tracking and Navigation with LEO Satellites," *Proceedings of the 34th International Technical Meeting of the Satellite Division of The Institute of Navigation (ION GNSS+ 2021)*, pp. 2507–2520, 2021.

32. B. McLemore and M. L. Psiaki, "Navigation using Doppler Shift from LEO Constellations and INS Data," *Proceedings of the 33rd International Technical Meeting of the Satellite Division of the Institute of Navigation, ION GNSS+ 2020*, pp. 3071–3086, 2020.

33. P. Misra and P. Enge, *Global Positioning System: Signals, Measurement, and Performance*, 2nd ed. Ganga-Jamuna Press, 2006, ch. 1-2.

34. J. Morales, J. Khalife, and Z. M. Kassas, "Simultaneous Tracking of Orbcomm LEO Satellites and Inertial Navigation System Aiding using Doppler Measurements," *IEEE Vehicular Technology Conference*, vol. 2019-April, no. 2, 2019.

35. J. J. Morales, J. Khalife, U. S. Cruz, and Z. M. Kassas, "Orbit Modeling for Simultaneous Tracking and Navigation using LEO Satellite Signals," *Proceedings of the 32nd International Technical Meeting of the Satellite Division of the Institute of Navigation, ION GNSS+ 2019*, pp. 2090–2099, 2019.

36. Space Debris and Human Spacecraft. NASA. Accessed: 2022-01-27. [Online]. Available: https://www.nasa.gov/mission_pages/station/news/orbital_debris.html

37. M. Neinavaie, J. Khalife, and Z. M. Kassas, "Exploiting Starlink Signals for Navigation: First Results," *Proceedings of the 34th International Technical Meeting*

of the Satellite Division of The Institute of Navigation (ION GNSS+ 2021), no. i, pp. 2766–2773, 2021.

38. M. L. Psiaki, "Navigation using carrier Doppler shift from a LEO constellation: TRANSIT on steroids," *NAVIGATION*, vol. 68, no. 3, pp. 621–641, 2021.

39. T. G. Reid, A. M. Neish, T. Walter, and P. K. Enge, "Broadband LEO Constellations for Navigation," *Navigation, Journal of the Institute of Navigation*, vol. 65, no. 2, pp. 205–220, 2018.

40. T. G. Reid, T. Walter, P. K. Enge, D. Lawrence, S. Cobb, G. Gutt, M. O'Connor, and D. Whelan, "Navigation from Low Earth Orbit," in *Position, Navigation, and Timing Technologies in the 21st Century.* John Wiley and Sons, Inc., 2020, vol. 2, ch. 43, pp. 1359–1412.

41. GPS: A $1.4 Trillion Economic Engine. RTI International. Accessed: 2022-01-26. [Online]. Available: https://www.rti.org/impact/gps-14-trillion-economic-engine#:~:text=We%20estimated%20that%20a%20complete,prolonged%20outage%20may%20be%20unlikely.

42. S. Thompson, S. Martin, and D. Bevly, "Single Differenced Doppler Positioning with Low Earth Orbit Signals of Opportunity and Angle of Arrival Estimation," pp. 497–509, 2021.

REPORT DOCUMENTATION PAGE

Form Approved
OMB No. 0704–0188

1. REPORT DATE *(DD–MM–YYYY)*	2. REPORT TYPE	3. DATES COVERED *(From — To)*
24–03–2022	Master's Thesis	Mar 2019 — Mar 2022

4. TITLE AND SUBTITLE

Performance Assessment of Navigation Using Carrier Doppler Measurements from Multiple LEO Constellations

5a. CONTRACT NUMBER

5b. GRANT NUMBER

5c. PROGRAM ELEMENT NUMBER

6. AUTHOR(S)

Hartnett, Michael J.

5d. PROJECT NUMBER

5e. TASK NUMBER

5f. WORK UNIT NUMBER

7. PERFORMING ORGANIZATION NAME(S) AND ADDRESS(ES)

Air Force Institute of Technology
Graduate School of Engineering and Management (AFIT/EN)
2950 Hobson Way
Wright-Patterson AFB OH 45433-7765

8. PERFORMING ORGANIZATION REPORT NUMBER

AFIT-ENG-MS-22-M-032

9. SPONSORING / MONITORING AGENCY NAME(S) AND ADDRESS(ES)

Combat Capabilities Development Command C5ISR Center
Dr. Gary Katulka
6586 Surveillance Loop
Aberdeen Proving Ground, MD 21005

10. SPONSOR/MONITOR'S ACRONYM(S)

DEVCOM C5ISR Center

11. SPONSOR/MONITOR'S REPORT NUMBER(S)

12. DISTRIBUTION / AVAILABILITY STATEMENT

DISTRIBUTION STATEMENT A.
APPROVED FOR PUBLIC RELEASE; DISTRIBUTION UNLIMITED.

13. SUPPLEMENTARY NOTES

14. ABSTRACT

The goal of this work is to characterize a novel navigation method which uses carrier Doppler shift measurements from LEO satellites. An ever-growing reliance on the GNSS has coincided with an increase in ways it can be degraded or denied, whether naturally occurring or man-made. These potentially disastrous threats to traditional navigation and timing have necessitated new technologies to augment GNSS in the case of an outage. LEO constellations, whose size and higher signal power make them potentially useful for navigation, are one technology that has been explored. The navigation algorithms detailed in this research use Doppler measurements from 8 or more LEO satellites to simultaneously solve for position, clock offset, velocity, and clock offset rate. Through simulation, a user-satellite geometry analysis is conducted for a number of emerging LEO constellations, as well as navigation simulations with the same constellations. Results are presented which show promise from both a satellite geometry perspective and PVT solution convergence perspective.

15. SUBJECT TERMS

Alternative navigation, signals of opportunity, low earth orbit

16. SECURITY CLASSIFICATION OF:			17. LIMITATION OF ABSTRACT	18. NUMBER OF PAGES	19a. NAME OF RESPONSIBLE PERSON
a. REPORT	b. ABSTRACT	c. THIS PAGE			Dr. Sanjeev Gunawardena, AFIT/ENG
U	U	U	UU	92	19b. TELEPHONE NUMBER *(include area code)* (937)-255-3636 x4659; Sanjeev.Gunawardena@afit.edu